Integration and Characterization of a Control and Signal Processing System for a SERF Magnetometer Array

By

Jeffrey Ryan Norell

B.S. Mechanical Engineering
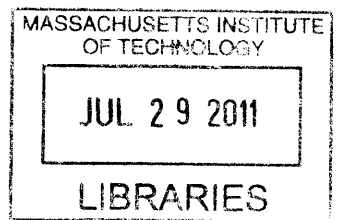Boston University College of Engineering, 2009

SUBMITTED TO THE DEPARTMENT OF MECHANICAL ENGINEERING IN PARTIAL
FULFILLMENT OF THE REQUIREMENTS FOR THE DEGREE OF

MASTER OF SCIENCE IN MECHANICAL ENGINEERING
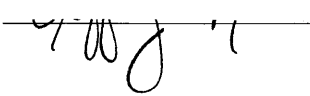AT THE
MASSACHUSETTS INSTITUTE OF TECHNOLOGY

JUNE 2011

©2011 Jeffrey Ryan Norell. All rights reserved.
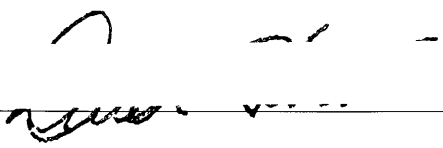
Signature of Author: _____

Department of Mechanical Engineering
May 2011

Certified by: _____

Joseph Kinast
Charles Stark Draper Laboratory
Thesis Supervisor

Certified by: _____

David L. Trumper
Professor of Mechanical Engineering
Thesis Supervisor

Accepted by: _____

David E. Hardt
Chairman, Department Committee on Graduate Students

1

[THIS PAGE INTENTIONALLY LEFT BLANK]

Integration and Characterization of a Control and Signal Processing System for a SERF Magnetometer Array

by

Jeffrey Ryan Norell

Submitted to the Department of Mechanical Engineering on
May 20, 2011, in partial fulfillment of the requirements for the
Degree of Master of Science in Mechanical Engineering

ABSTRACT

Interest in the development of ultrasensitive magnetometers is driven by applications in a variety of areas, including magnetoencephalography (MEG), magnetic anomaly detection (MAD), dynamic measurements of geomagnetic fields, and MRI signal detection. While numerous architectures are being pursued in the development of high sensitivity magnetometers, optical atomic magnetometers are of substantial interest due to their small size and promising performance characteristics. In particular, spin exchange relaxation free (SERF) magnetometers have demonstrated ultimate flux density measurement sensitivities of 10^{-15} Tesla/Hz$^{1/2}$, with projected fundamental sensitivity limits orders of magnitude lower. In this thesis, I describe the development and characterization of an integrated control and signal processing system for an array of SERF magnetometers. In particular, I address the integration and control of optical, magnetic, and electronic subsystems required for operation of an array of 64 independent SERF magnetometers. Additionally, I detail a testing regimen to verify proper operation of each subsystem and characterize the performance of a single SERF magnetometer operated by our integrated control and signal processing system.

Technical Supervisor: Joe Kinast
Title: Technical Staff, Charles Stark Draper Laboratory

Thesis Advisor: David L. Trumper
Title: Professor of Mechanical Engineering

[THIS PAGE INTENTIONALLY LEFT BLANK]

Acknowledgements

I would like to give my deepest thanks for all of those who have helped with my master's work. First, I would like to thank Draper Laboratory for the opportunity to complete my master's degree at MIT and for providing all facilities and resources used to complete this research. As a graduate student, Draper provides great facilities, expert personnel, and exceptional support. I would like to thank all of department GBE1 and especially Tony Radojevic for hiring me on and providing answers to my questions during the beginning of the program.

My deepest thanks go to Joe Kinast, my Draper supervisor, for taking over the role as my technical advisor and answering my many, many questions. Joe also took the time to thoroughly revise my thesis as well as take many road trips to assure that critical equipment was received with enough time for me to complete my research. Without him, completion of my research would not have been possible.

I would like to thank Professor Romalis from Princeton University for his role as principal investigator of the HUMS program and for finding Draper Laboratory a suitable partner in his research. Without his continued advancement of optical magnetometry my research would not be possible.

Thanks goes out to Tom Kornak of Twinleaf LLC, as well as the staff at Agiltron Inc for answering many of my questions over the last two years. Peter Milne of D-Tacq Solutions also assisted greatly with his support of the custom acquisition system.

I would also like to thank Professor David Trumper for taking time out of his very busy schedule to provide valuable feedback and suggestions for this thesis.

Finally, I would like to thank all my family and friends for their continued support over the years, and for putting up with my crazy schedule when deadlines were approaching. Without their continued support I would not be where I am today.

[THIS PAGE INTENTIONALLY LEFT BLANK]

Table of Figures

Chapter 1 – Introduction

1.1 Background

Ever since the first compass was invented over 2000 years ago, magnetic fields and their measurement have played a large part in the development of society and in the advancement of technology. The compass was used in the 12th century B.C. by the Chinese, and later the Europeans, to navigate and explore parts of the world previously unknown to them [1]. Then, in the 1830s Carl Friedrich Gauss began investigating the theory of terrestrial magnetism and published three papers on the subject. He also invented the first magnetometer, a device for measuring the strength of a magnetic field [2]. The first magnetometer was simply a suspended bar magnet; in the intervening years, magnetometers have grown in complexity and achieved remarkable sensitivity.

A magnetometer is simply an instrument that measures magnetic fields. They are present in many different aspects of the modern world, ranging from cell phone internal compasses and metal detectors to aircraft and satellite navigation. There is currently substantial interest in improving the measurement capabilities of magnetometers driven by applications that require very high precision and sensitivity. These include magnetoencephalography (MEG), magnetic anomaly detection (MAD), magnetic resonance imaging (MRI), and dynamic measurements of geomagnetic fields, among others [3].

Figure 1: Magnetometer installed on the back of a P-3C aircraft for MAD[1]

1.2 Introduction to Magnetometers

There are three basic ways a magnetometer can measure magnetic fields. Vector magnetometers measure field strength in one direction and are the most widely used in navigation for automobiles, aircraft, and spacecraft. Scalar magnetometers measure the total magnitude of the magnetic field and are useful for magnetic anomaly detection (MAD) and have also been used to map the earth's field. Radio

---

[1] Taken from commons.wikimedia.org (a freely licensed media repository)

frequency (RF) magnetometers measure transverse magnetic fields at a tuned frequency ω and are useful for detecting radio waves as well as nuclear magnetic resonance (NMR) and nuclear quadrupole resonance (NQR) measurements [4]. There are also many different magnetometer designs in use today. The most common sensors include Hall Effect sensors, fluxgate magnetometers, magnetoresistors, superconducting quantum interference devices (SQUIDs) and the recently developed spin exchange relaxation free (SERF) magnetometers.

Hall Effect sensors rely on a thin semiconductor that when driven by an excitation current generates a voltage potential when placed in a magnetic field. They are generally cost-effective and are typically used as proximity sensors, for position measurement (for example, gear angle measurement), and can be used for current sensing. They are not used for high sensitivity measurements[2] due to their limited sensitivity of approximately 1 nT/√Hz but have a bandwidth of anywhere from DC to 30kHz depending on design [5].

Fluxgate magnetometers are substantially more sensitive than Hall Effect sensors (up to ~1pT/√Hz). They are used extensively in aircraft and vehicle navigation systems because they function as a vector magnetometer. The sensor itself is a solid state device that consists of a ferromagnetic core surrounded by an excitation coil and an inductance coil. The core is excited by an AC current passed through the excitation coil. If a DC magnetic field is also present, the core flux changes and there is an induced voltage in the inductance coil which can be scaled to a magnetic field measurement. Fluxgate magnetometers are also very temperature stable and have a bandwidth of anywhere from a few hertz to three kilohertz.
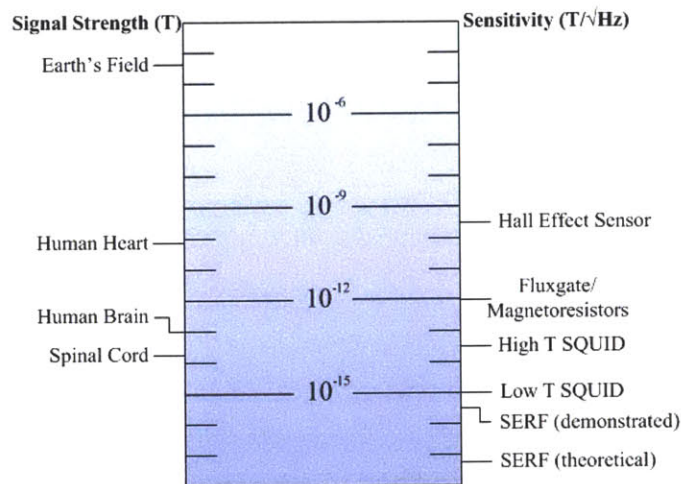
Figure 2: Comparison of different magnetometer sensitivities[3]

[2] Magnetic noise is often represented as the square root of the power spectrum at a given frequency and typically given in units of nT/√Hz or pT/√Hz [4].
[3] Adapted from [8], pg 6

Magnetoresistors are materials that change electrical resistance in the presence of a magnetic field. There are two general types of magnetoresistors: ordinary magnetoresistors (OMRs) consist of thin films of ferromagnetic materials and have a maximum resistance change of 5% in the presence of magnetic fields, while giant magnetoresistance (GMR) detectors consist of sandwiches of ultrathin magnetic and nonmagnetic layers and can have a resistance change of more than 10%. Magnetoresistors generally have good temperature stability, a measurement bandwidth from DC to approximately 100MHz, and a maximum resolution of 1nT [5]. The use of a thin film to measure flux density also results in a sensor that is sensitive to magnetic field direction. GMRs are often used in the magnetic read heads of hard disk drives.

The most sensitive magnetometer in widespread use today is the superconducting quantum interference device (SQUID). SQUIDs can operate as vector or RF magnetometers and rely on a Josephson junction (a weak link between two superconductors that allows a maximum current to pass without a voltage drop) connected to a superconducting loop. A change in magnetic flux through the Josephson junction results in a change in voltage. Through lock-in detection, the voltage versus magnetic flux relationship can be linearized, and maximum sensitivities of $1fT/\sqrt{Hz}$ are possible. Unfortunately, measuring at high sensitivities in the background magnetic field generated by the earth is impossible with modern electronics due to a required 200 dB dynamic range[4]. Consequently, high sensitivity measurements must be performed in magnetic shields. However, SQUIDs do have a very large bandwidth that can range from a few hertz to approximately 30 kHz. SQUIDs typically operate at the temperature of liquid helium (approximately 4.2K) for a low-temperature superconductor and the temperature of liquid nitrogen (approximately 77K) for a high temperature superconductor. To conduct high-sensitivity measurements, SQUIDs require a large insulated cryogenic chamber along with a steady supply of coolant. As a result, they are far from ideal for portable measurements.

---

[4] (earth's field of $100\mu T$)/($10fT$ sensitivity) = 200 dB dynamic range

13

1.3 SERF Magnetometers
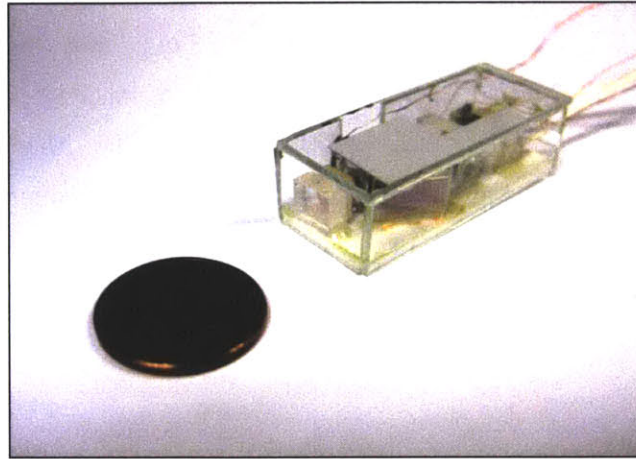
Figure 3: Full SERF Magnetometer Sensing Head Next to a Penny

Spin Exchange Relaxation Free (SERF) magnetometers are a more recently developed technology that originated at Princeton University in Michael Romalis' research group [6]. SERF magnetometers use high density alkali vapors to measure magnetic fields. In some regimes they outperform SQUIDs (at measuring low magnitude magnetic fields) and do not require bulky supporting infrastructures such as cryogenic chambers. SERF magnetometers generally operate best at elevated temperatures (greater than 100°C) but they can operate in a reduced sensitivity low-power mode at room temperature, and have a small package size. SERF magnetometers are presently in the research stage but have already demonstrated sensitivities of less than $1fT/\sqrt{Hz}$ [3]. The SERF sensor itself consists of a small heated glass cell filled with an alkali vapor (see Figure 4). Linearly polarized laser light is fed into the vapor cell and polarizes the alkali atoms. As a magnetic field is applied to the atoms, their atomic spins precess about the magnetic field. A separate linearly polarized probe beam then passes through the cell and undergoes polarization rotation due to the state of the atoms. This measured polarization can then be scaled to yield magnetic field measurements. The fundamental sensitivity of these sensors (using potassium in the vapor cell) is approximately $10^{-17}V^{-1/2}\,T/\sqrt{Hz}$, where V is the volume of the vapor cell in cubic centimeters [3]. In our application the cell volume is $0.125cm^3$, which results in a fundamental sensitivity on the order of $0.03fT/\sqrt{Hz}$.
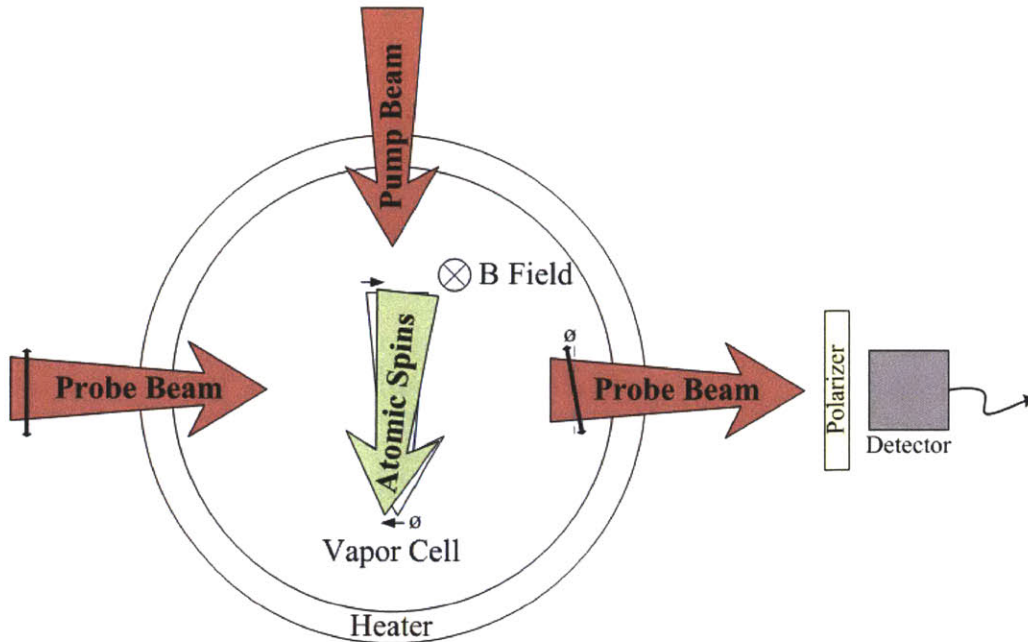
Figure 4: General Schematic of a SERF Magnetometer

Another benefit of SERF magnetometers is that they can perform the three main types of magnetic field measurements with very little change to their setup. The magnetometer can act as a vector magnetometer, a scalar magnetometer, and a radio frequency (RF) magnetometer. All three measurements rely on the polarization of the probe beam to determine field strength. The only difference between the three modes is the modulation of the pump beam and modulation of the sensor's surrounding magnetic field (which is controlled through external electromagnetic coils). Recent experiments with an atomic RF magnetometer have also demonstrated high sensitivity at frequencies up to 50MHz[7]. Therefore, a SERF magnetometer allows for a large amount of flexibility with little change in design. The only major drawback of a standard scalar or vector SERF magnetometer is that operation requires a near-zero magnetic field. Therefore, the sensor must always have a passive magnetic shield and/or active electromagnetic coils to null the effects of earth's magnetic field. However, calibration of the sensor is determined only by fundamental constants and is thus not dependent on the specific operating environment.

1.4 Required Subsystems

Although SERF magnetometers are small and relatively simple to set up, they still require multiple subsystems for proper operation. Both the pump and the probe laser require an optical train and control scheme to modulate and control the temperature, power output, and polarization of the lasers. A control scheme and power source is required to operate the heaters and control the temperature of the cell to

ensure optimal temperature. The sensor's surrounding field coils need to null the earth's magnetic field and apply modulation to perform sensitivity measurements. A data acquisition system is required to measure and record all output from the sensor. Finally, a computer is needed to tie all systems together and act as a central control hub for the user. These control subsystems are the focus of this thesis and will be described in greater detail in subsequent chapters.

1.5 Proposed Sensing Array

Their high sensitivity, large amount of flexibility, and small size makes SERF magnetometers ideal for developing sensing arrays with multiple magnetometers. An array of sensors will allow for gradiometer-type measurements and will have the capability to perform measurements over a larger area than a single sensor. This will prove useful in real world applications such as magnetoencephalography (MEG) or monitoring of the human heart.

The intent of this research was to design, assemble, and test the integrated control and data acquisition system for an ultra-sensitive laser magnetometer array. Laser magnetometers are some of the most sensitive magnetometers in development today. However, as mentioned previously each sensor requires many subsystems for proper operation and all must be functioning properly to ensure peak performance of the magnetometer. Also, in the past, most designs consisted of a single isolated sensor. There are many additional challenges when designing a control system for a full sensing array. The design and performance verification of the optical, magnetic, and electric subsystems required for a proposed 64 sensor array will be discussed in more detail in this thesis.

Chapter 2 – System Control and Data Processing System

2.1 System Overview

The system development and integration described in this thesis was conducted under the Defense Advanced Research Projects Agency (DARPA) Heterostructural Uncooled Magnetic Sensors (HUMS) program. The HUMS program targets the development of room temperature, low frequency sensing arrays with SQUID-like performance that can be used for applications such as through-wall imaging and tagging/reading applications that require small deployable sensors. SERF magnetometers are an ideal sensor for this application due to their small size, high sensitivity, and lack of cryogenic cooling requirements. Charles Stark Draper Laboratory has partnered with Dr. Romalis at Princeton University, a Princeton startup named Twinleaf LLC, and Agiltron Inc to participate in the program. In the program, Princeton and Twinleaf are responsible for the SERF sensor head research and development, Agiltron is responsible for the optics and custom electronics manufacturing, and Draper Laboratory is responsible for the data acquisition (DAQ) and control system as well as overall system verification and integration.

As mentioned in the introduction, many subsystems are required for operation of a SERF magnetometer. Due to the multiple suppliers, care must be taken to assure that all equipment functions well together to ensure optimal sensor performance. Below is an overview of the components and interfaces necessary for a 64 sensor array.
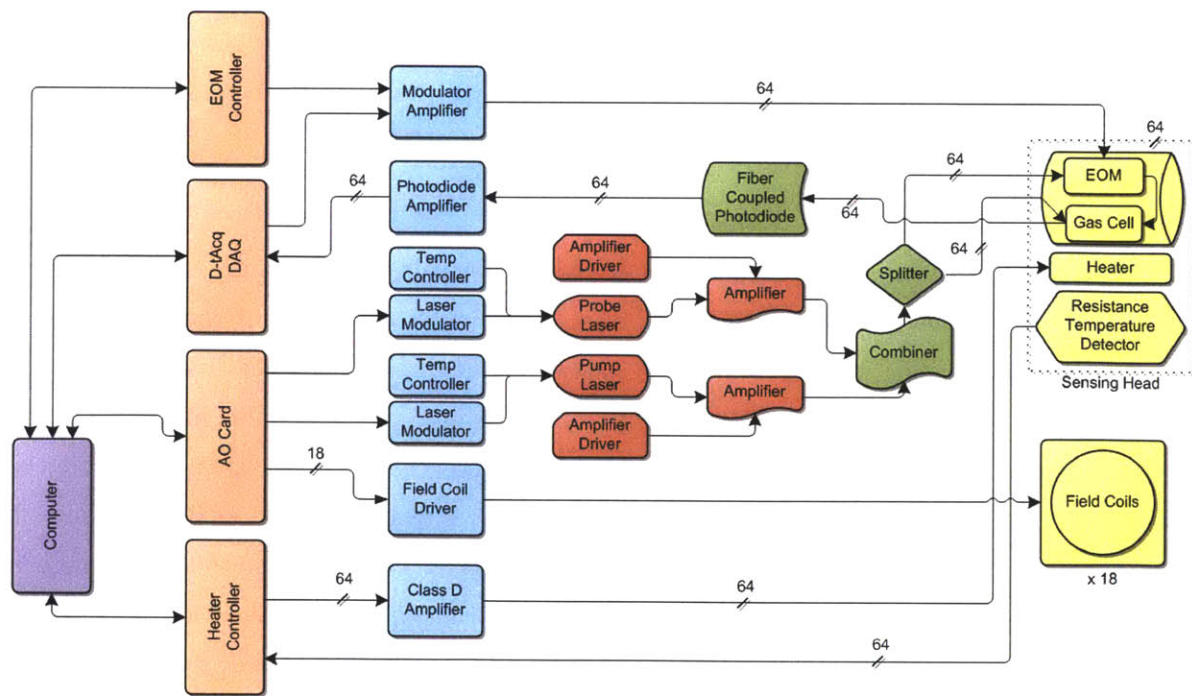
Figure 5: SERF magnetometer array: Full system overview

From this diagram one can see that almost all subsystems interface with a central computer, either directly or indirectly. It is crucial that the heater controller, the data acquisition system, and analog output card all function efficiently and operate deterministically when connected to the central computer. Figure 6 provides a very basic demonstration of what steps a user would take to set up and use the sensing system. Every step except for powering the lasers is performed through the PC, and all must function properly for optimal sensor performance.
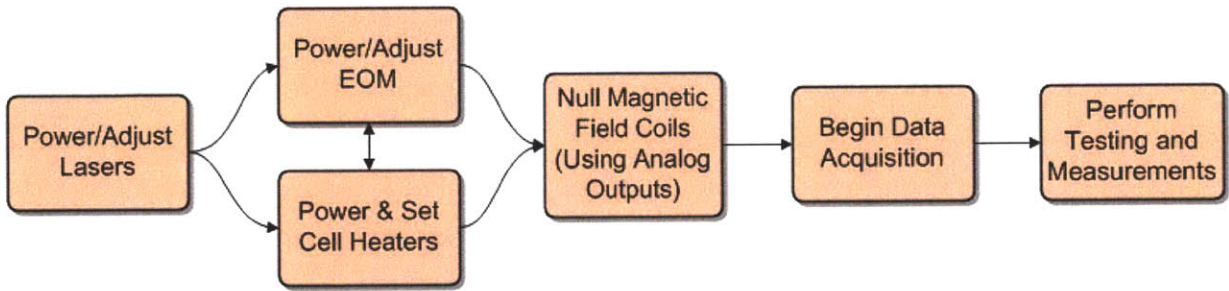
Figure 6: Basic System Flow Diagram

The remainder of this chapter focuses on the acquisition system and is organized as follows: in Section 2.2.1 I discuss the data acquisition system specifications. In Section 2.2.2 I discuss the acquisition hardware validation and performance testing. In Section 2.2.3 a noise analysis performed on the hardware is described.

2.2 Data Acquisition System

The data acquisition system (DAQ) is responsible for recording the real-time signal from all sensors simultaneously. No data can be lost and all data must possess the correct timestamps to accurately assess the performance of the sensors.

2.2.1 Specifications

The data acquisition system should accurately record the data from the sensors as well as allow for diagnostics and debugging of the sensors. Due to the small magnitude of the magnetic field signatures, lock-in detection is used to make all measurements. Lock-in detection is a measurement technique that allows for low-noise measurement of very small signals and is therefore ideal for our ultra-sensitive magnetometers. It involves manipulating an experimental variable at a fixed reference frequency and monitoring the experimental response at the reference frequency. Because only the response is measured at the reference frequency, noise sources at frequencies outside a narrow band around the reference are rejected by the amplifier. Most lock-in amplifiers also have two internal mixers that have the reference frequency 90 degrees out of phase from each other. This allows for measurement of both the amplitude and phase difference between the input and reference signals. For this reason lock-

18

in amplifiers are also called phase sensitive detectors. The reader is encouraged to read [8] for a good background tutorial on lock-in amplification.

In our sensor application, lock-in detection requires the input signal to the sensor (in this case the probe beam) to be modulated at a much higher frequency ω than the desired measurement bandwidth. This is done with a photoelastic optical modulator (also called an electro-optic modulator) and a series of optical wave-plates that result in an output beam intensity of [9]

$$I = I_0 \sin^2[\phi + \alpha \sin(\omega t)]$$

where α is the modulation amplitude and ϕ is the polarization rotation to be measured (which is a small angle proportional to magnetic flux density. For more a more detailed description of optical modulation see Section 5.3). Both α and ϕ are small, as large rotation angles result in a nonlinear signal [9], so $[\phi + \alpha \sin(\omega t)]$ is also small. Let

$$[\phi + \alpha \sin(\omega t)] \equiv A.$$

Then

$$I = I_0 \sin^2(A).$$

Taking a Taylor expansion about A = 0 results in

$$I \approx I_0 A^2 = I_0 [\phi + \alpha \sin(\omega t)]^2$$

$$= I_0 \{ \phi^2 + 2\alpha\phi \sin(\omega t) + \alpha^2 \sin^2(\omega t) \}.$$

Through use of the trigonometric identity $\sin^2(\omega t) = \frac{1}{2} [1 - \cos(2\omega t)]$ this can be rewritten as

$$I = I_0 \{ \phi^2 + 2\alpha\phi \sin(\omega t) + \frac{\alpha^2}{2} [1 - \cos(2\omega t)] \}.$$

This results in an output signal from the sensor that can be estimated as

$$I = -I_0 \frac{\alpha^2}{2} \cos(2\omega t) + 2I_0 \alpha\phi \sin(\omega t) + I_0 (\phi^2 + \frac{\alpha^2}{2}).$$

The first harmonic (fundamental) of the output signal contains the main signal, which will be demodulated through lock-in detection and can then be calibrated to magnetic field strength. The demodulated DC component and second harmonics of the output signal also provide helpful diagnostic

19

information. For this reason the data acquisition system features custom hardware with 5-way lock-in demodulation. The hardware outputs a signal on the order of twenty kilohertz that is used to modulate the probe laser signal. The input signal can be independently demodulated to an average value (essentially low-pass filtering the data) as well the $\sin(\omega)$, $\cos(\omega)$, $\sin(2\omega)$, and $\cos(2\omega)$ magnitude components of the system response to the modulation frequency. The phase of the signal can be determined from the magnitude difference of orthogonal components (although in typical operating conditions, the output signal's phase will be adjusted to put all signal in either the $\sin(\omega)$ or $\cos(\omega)$ reference component).

The desired characteristics for the acquisition system were specified by Princeton University as they are the end user of our control and acquisition system. The acquisition rate needed to be at least 200Hz and a rate between 500Hz and 1 kHz was preferable to achieve a larger sensing bandwidth. In addition to providing data acquisition capabilities, the system also needed to output the lock-in reference signal as well as 18 analog out signals to control the sensor's background nulling magnetic coils. Finally, to greatly simplify magnetic field measurement the output reference signal also needs to be phase adjustable. This permits nulling of the $\cos(\omega)$ lock-in output and allows for full signal measurement on the $\sin(\omega)$ reference.

After researching many manufacturers, a custom acquisition system from D-tacq Solutions (located in Scotland, UK) was selected for the SERF sensor array. D-tacq Solutions was willing to build a custom acquisition PCI card with five-way references available on 64 channels (based off of part number ACQ196PCI). There are also 32 channels with one-way reference capabilities for general purposes such as temperature monitoring. These channels can also be switched to 5-way references if desired. The system is ideal for the sensing array due to its scalability. Because the acquisition system consists of PCI cards that are chassis mounted, a total of 4 acquisition boards can be run simultaneously with the existing system. This would allow for a sensing array of up to 384 sensors (96 channels x 4 acquisition cards) with no significant changes in the existing data acquisition design. The system also has a maximum sample throughput of 500 kHz before lock-in processing, has a 16-bit analog to digital converter, and has an advertized signal-to-noise ratio of 86dB (with a full-scale differential input). Because SERF magnetometers must operate in a field of less than ~10nT [3] this 16-bit input results in an electronics limited resolution of 153fT when configured to measure maximum possible magnetic field[5]. If the desired resolution is 0.1fT, a maximum measurement of 6.5pT is possible. These performance specifications were deemed acceptable by Princeton University.

---

[5] $10^{-8}T/2^{16} = 153 \times 10^{-15}$ T resolution

2.2.2 Validation

Due to its custom nature, the functionality of the data acquisition system lock-ins needed to be verified. Additionally, both throughput and sensitivity performance needed to be assessed. Throughput performance was specified to be at least 200Hz with 500-1000Hz preferred with all lock-ins enabled. The throughput is simply the acquisition clock rate divided by the integration length. Consequently, throughput can be controlled on the acquisition cards by adjusting either the acquisition clock rate or the lock-in amplifier integration length.

For all testing the clock rate was left on its highest available setting (501,253Hz) and the integration length was changed until the card missed samples or stopped sending data all together. Initial testing gave us a maximum throughput rate of 501Hz at an integration length of 1000. At rates higher than this the D-tacq cards froze and required a hard reset. Also, the Ethernet transceiver the cards were sending data over is capable of 10Mbit/sec. Consequently, a 501Hz indicated a data flow rate of

$$(64 \, \text{Channels} \times 5 \, \text{References} + 32 \, \text{Channels} \times 1 \, \text{Reference}) \times 16 \frac{\text{bit}}{\text{sample}} \times 501 \frac{\text{samples}}{\text{second}}$$

$$= (358) \times 8016 \frac{\text{bits}}{\text{second}} = 2.9 \frac{\text{Mbits}}{\text{sec}},$$

which is only about 30% of the maximum theoretical transfer rate. Discussions with the manufacturer revealed that there was a problem with the card's firmware. There were not enough data transfer buffer objects present on the card, which would overfill at higher transfer rates and result in the card crashing. The manufacturer changed the number of objects in updated firmware and further testing revealed that the card was capable of a maximum throughput of 1,671Hz with all lock-ins enabled. This corresponds to a data transfer rate of

$$(358) \times 16 \frac{\text{bit}}{\text{sample}} \times 1671 \frac{\text{samples}}{\text{second}} = 9.6 \frac{\text{Mbits}}{\text{sec}},$$

which also does not account for any other network traffic. This is the maximum data transfer rate that the current Ethernet implementation is capable of, but is well over the specified system requirements. The throughput of the card can also be increased by decreasing the number of references per channel. A maximum throughput of 6,266Hz was demonstrated with only one lock-in reference on all 96 channels.

The lock-in functionality of the acquisition system also needed to be demonstrated. This was performed with a simple multiplication circuit that simulated the basic output from a sensor (see Figure 7 and Figure 8).
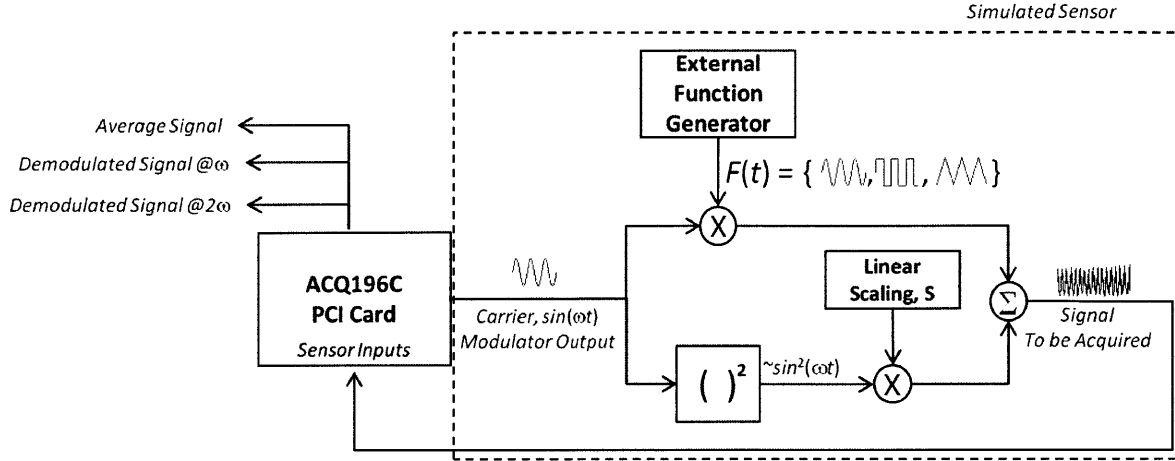
Figure 7: Functional Block Diagram of Simulated Sensor for Testing

This circuit takes the reference frequency from the acquisition cards, multiplies it by an arbitrary waveform supplied by a separate source, and then adds in a second harmonic reference component. This signal is then fed back into the acquisition cards for lock-in demodulation and is in the form

$$\Sigma = F(t)\sin(\omega t) + S\sin^2(\omega t)$$

To verify functionality of the lock-in demodulation, an arbitrary sinusoid, sawtooth wave, and square wave were fed into the circuit as F(t) and modulated by the first harmonic. Simple amplitude scaling was also performed on the $\sin^2(\omega t)$ component, which is linearly proportional to the second harmonic by the trigonometric identity

$$\sin^2(\omega t) = \frac{1 - \cos(2\omega t)}{2},$$

which leads to a signal output in the form

$$\Sigma = -\frac{S}{2}\cos(2\omega t) + F(t)\sin(\omega t) + \frac{S}{2}.$$

Both the second harmonic and DC component should scale linearly with changes in the scaling factor S. The first harmonic of the signal will only respond to changes in the applied signal F(t). This is of the same functional form as the measured intensity output of the physical sensing head (derived in the beginning of this section)

$$I = -I_0\frac{\alpha^2}{2}\cos(2\omega t) + 2I_0\alpha\phi\sin(\omega t) + I_0(\phi^2 + \frac{\alpha^2}{2}).$$

One can see that the physical coefficients corresponding to magnetic measurement, $I_0\alpha\emptyset$, are simulated by input from a function generator, F(t). However, the DC component of the intensity signal will also be affected by changes in rotation, ø.

22

This amplitude scaling was performed by changing resistors on a voltage multiplier in the circuit. Actual output voltage scaling S was not directly measured due to the modulation effects from the circuit. However, resistors were chosen that resulted in a scaling of unity (1), a scaling of 0.5, and a scaling of 0.33. Data was then recorded for the average, sin(ω), and sin(2ω) lock-in references for each combination of arbitrary waveforms and resistor values.
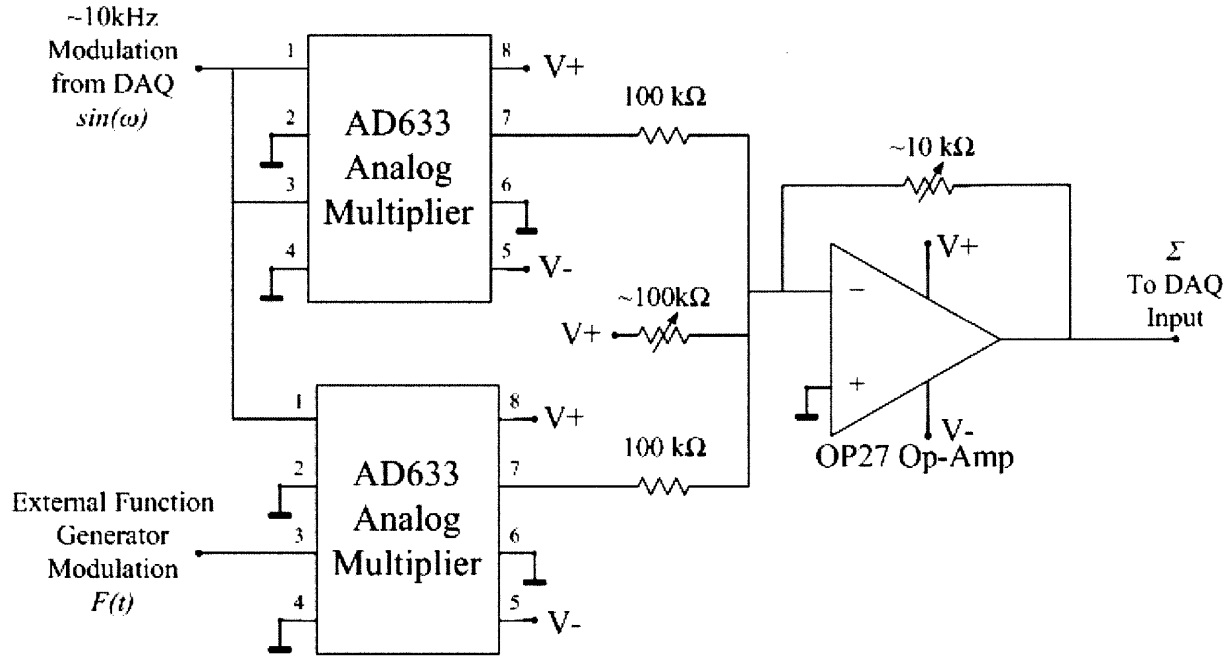
Figure 8: Circuit Schematic of Simulated Sensor for Testing

As expected, both the average and the second harmonic lock-in result in DC outputs that scale linearly with the voltage offset (due to the scaling factor S, provided by the resistors). The arbitrary waveform input has no effect on their values. Further, the first harmonic lock-in outputs the demodulated arbitrary waveform with no effect from changes in DC offset. The results validate the functionality of the custom lock-in electronics and are displayed in Figures 9 – 11. The top row of plots in each figure displays the output from the average reference and scales linearly with the scaling factor S. The second row of plots shows the output from the sin(ω) reference, which does not change with DC offset due to the scaling factor. Finally, the last row of plots shows the demodulated output from the cos(2ω) reference, which also scales linearly with the scaling factor. These results conceptually demonstrate that the lock-in amplifier is functioning as expected.
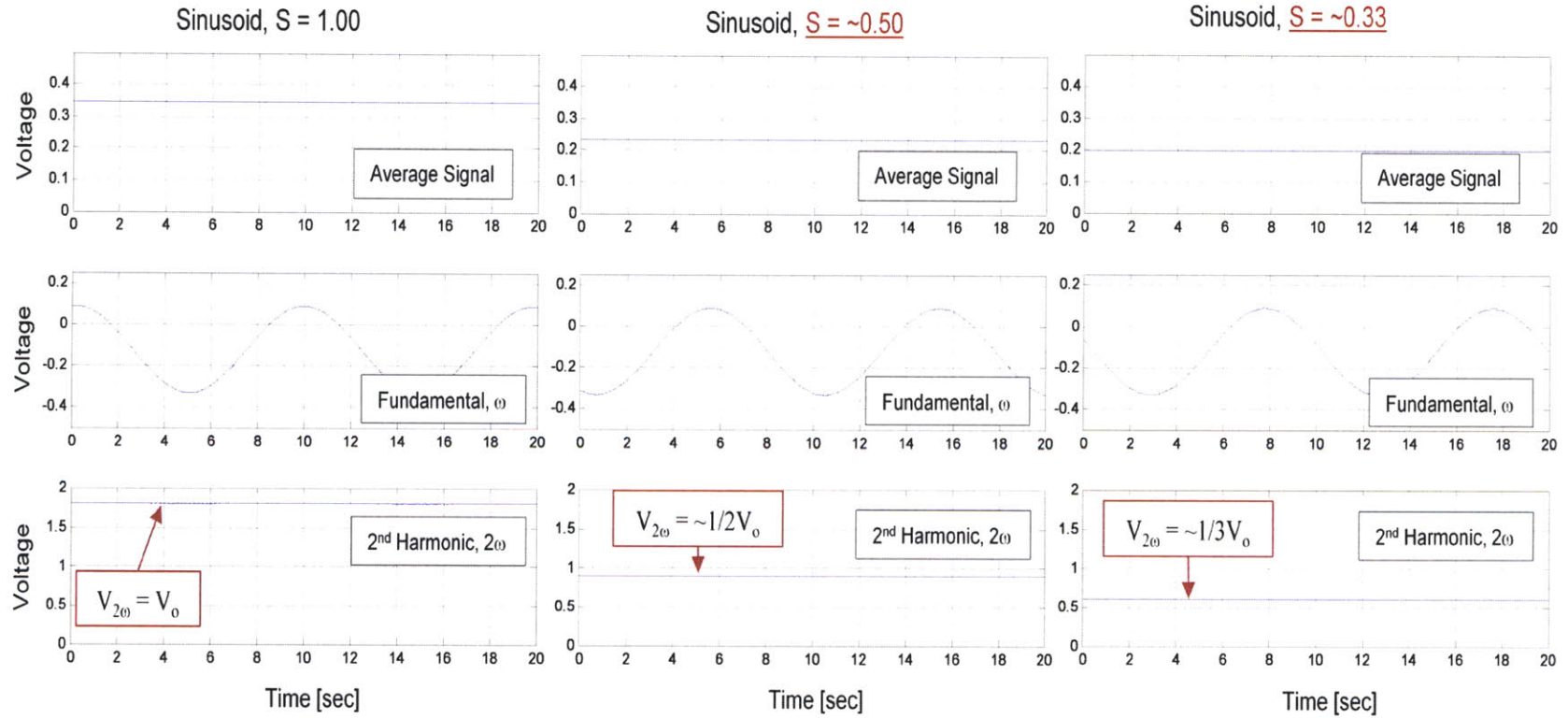
Figure 9: Sinusoid Testing of Lock-in Functionality
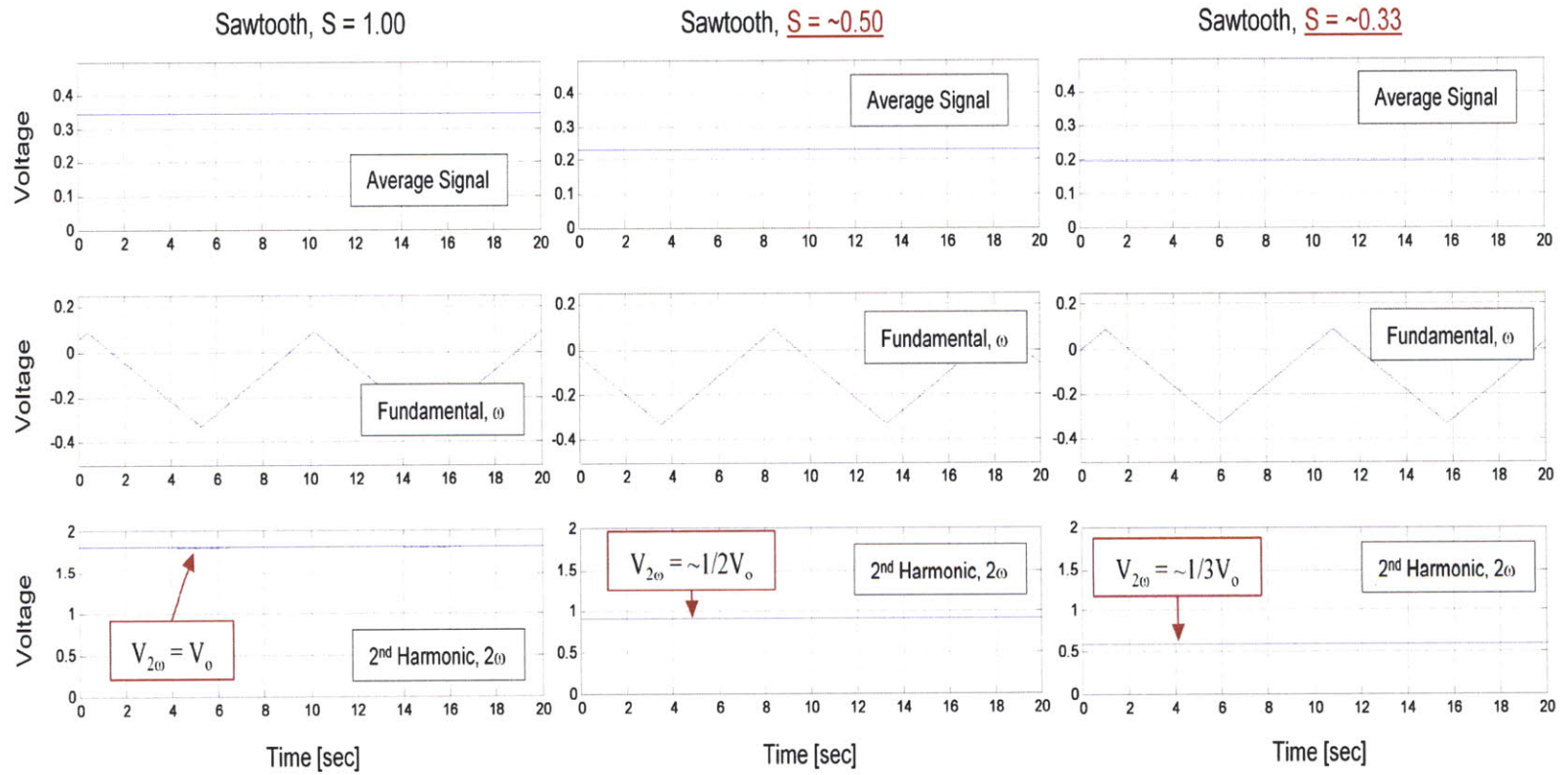
Figure 10: Sawtooth Testing of Lock-in Functionality

Square Wave, S = 1.00   Square Wave, S = ~0.50   Square Wave, S = ~0.33

Average Signal

Fundamental, ω

2nd Harmonic, 2ω

$V_{2\omega} = V_o$

$V_{2\omega} = \sim 1/2 V_o$

$V_{2\omega} = \sim 1/3 V_o$

Time [sec]
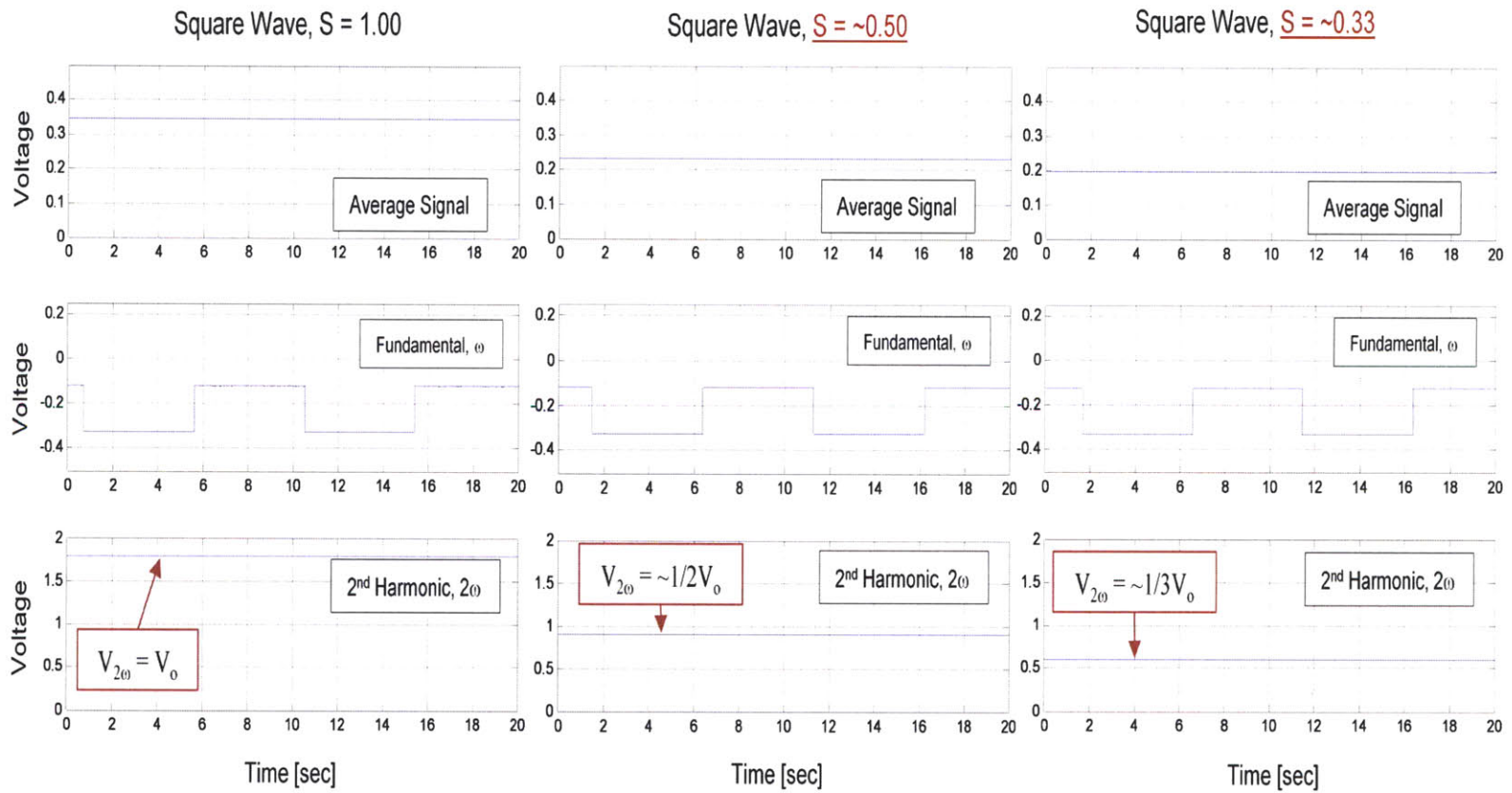
Figure 11: Square Wave Testing of Lock-in Functionality

26

2.2.3 Hardware Noise Analysis

The signal-to-noise ratio (SNR) is simply the ratio of full-scale input signal (σ) to the noise level (N) of the instrumentation and can be expressed in dB as

$$\text{SNR} = 20\log\left(\frac{\sigma}{N}\right),$$

with the signal at its maximum amplitude for the given hardware. The signal to noise ratio is useful for determining the hardware limited measurement range of the sensor. Another performance metric of interest is the noise floor of the hardware. The noise floor is the sum of all electronic noise sources and can be easily found by taking the fast Fourier transform (FFT) of an input signal and removing the input frequency and its resulting harmonics. This results in a pure noise spectrum that is equivalent to the noise floor. This allows us to discern what noise in the final sensor measurement is associated with the hardware and which is from other system sources such as the lasers or electrical noise in the wires.

To assess the system's noise levels multiple methods were used. First, the inputs to the acquisition system were shorted together to determine the noise floor. This data was recorded at 500Hz over a period of five minutes. It was then analyzed in MATLAB and the FFT was taken (with no windowing to skew the data). The magnitude of the FFT output was then plotted against frequency. The resulting plot is the measured noise floor of the electronics plus the FFT process gain (see Figure 12).
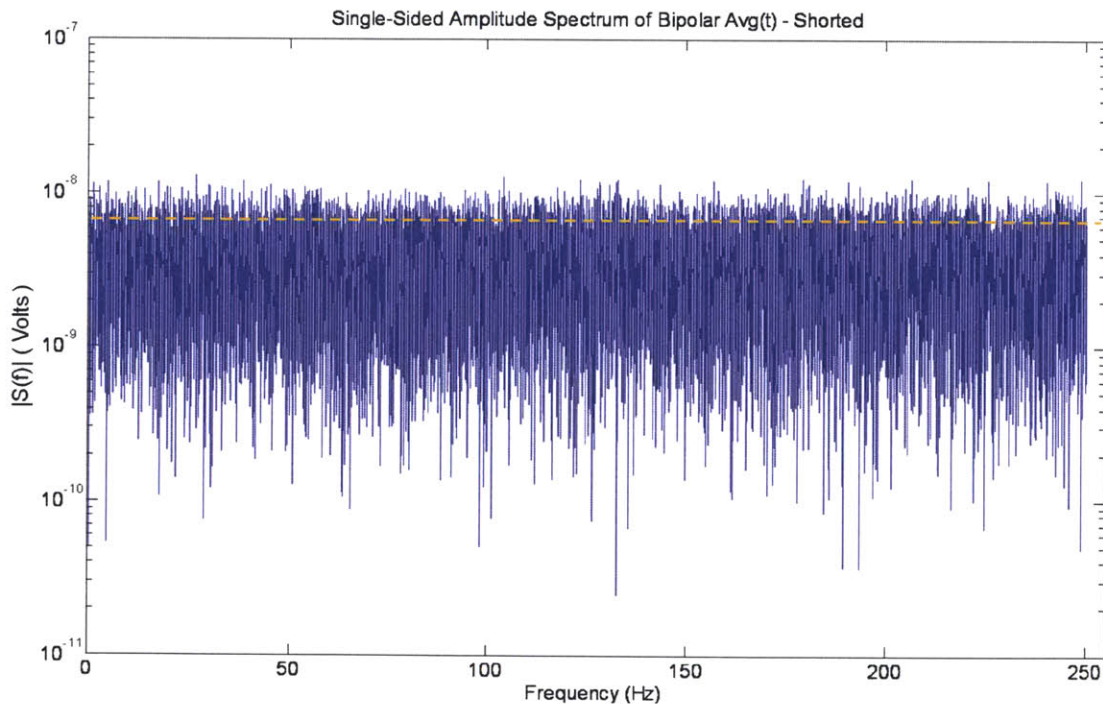
Figure 12: FFT Process Gain plus Noise Floor of Acquisition System Input

27

The FFT process gain is a very important factor to consider in signal to noise calculations. Due to the algorithm used to calculate the Fourier transform, the FFT acts as a narrowband spectrum analyzer with a bin width of $f_{sampling}/M$ (where M is the number of points used to calculate the FFT). This bin width is also known as the resolution of the FFT. The output from the FFT sweeps over the Nyquist bandwidth of the instrument (DC to one-half the sampling frequency) [10][11]. This results in the noise being pushed down by the FFT process gain, $10\log(M/2)$ dB. Since the noise floor FFT in this analysis was taken with 150,000 points, the FFT process gain is

$$10\log\left(\frac{150000}{2}\right) = 48.75\text{dB}$$

.

At full range input of 10 Volts, this yields an ultimate noise floor of

$$20\log\left(\frac{\text{Full Range Signal}}{\text{FFT Noise Floor}}\right) - \text{FFT Process Gain} = 20\log\left(\frac{10}{4\times10^{-9}}\right) - 48.75\,\text{dB} = 139\,\text{dB}$$

.

Next, a 5VDC signal from an external function generator was modulated by a 10 kHz reference frequency from the acquisition system using the circuit mentioned in Section 2.2.2 of this chapter. The data was processed by both the average and $\sin(\omega)$ lock-ins on the hardware and the FFT calculated in Matlab to view the noise reduction characteristics of the lock-ins. These spectra are displayed in Figure 13 and Figure 14. In both cases, the baselines are on the order of $1\mu V$.
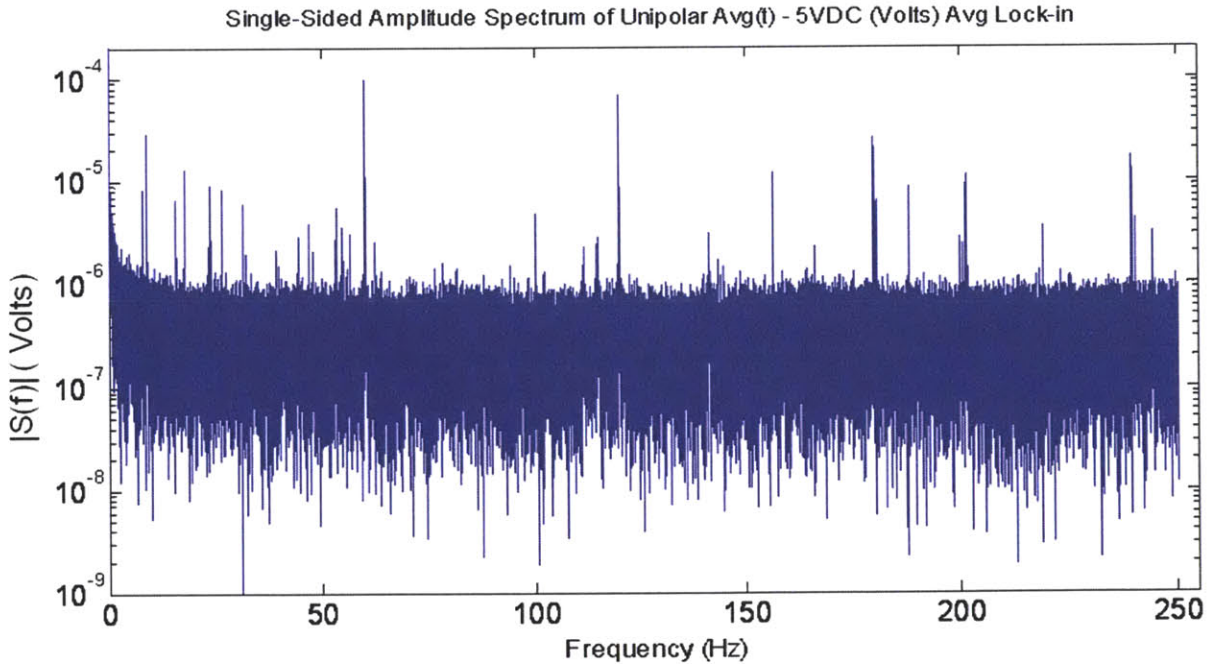
Figure 13: 5VDC, 10 kHz modulated: Average lock-in

28

Single-Sided Amplitude Spectrum of Unipolar Avg(t) - 5VDC (Volts) - SINW Lock-In
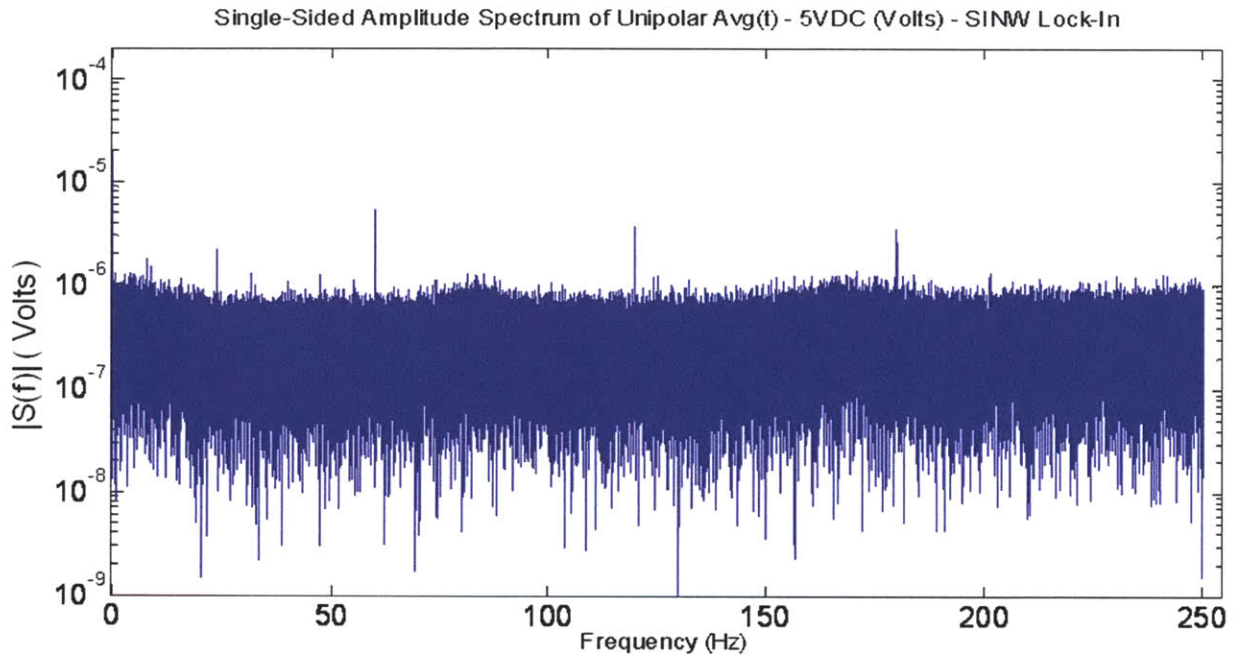
Figure 14: 5VDC, 10 kHz modulated: Sin(ω) lock-in

It was realized after taking data that the circuit used to modulate and multiply the signals contained many additional sources of technical noise, as can be seen in the plots. However, this data still clearly demonstrates the benefits of the lock-in processing. There is much more noise evident in the average processed plot (Figure 13) as opposed to the sin(ω) lock-in plot (Figure 14). This is because the averaging acts a simple low-pass filter, while the sin(ω) lock-in modulation removes all of the noise except for some 60Hz electrical noise and its higher order harmonics. The sin(ω) locked-in signal also shows reduced $1/f$ noise at low frequencies, as can be seen clearly in Figure 15.
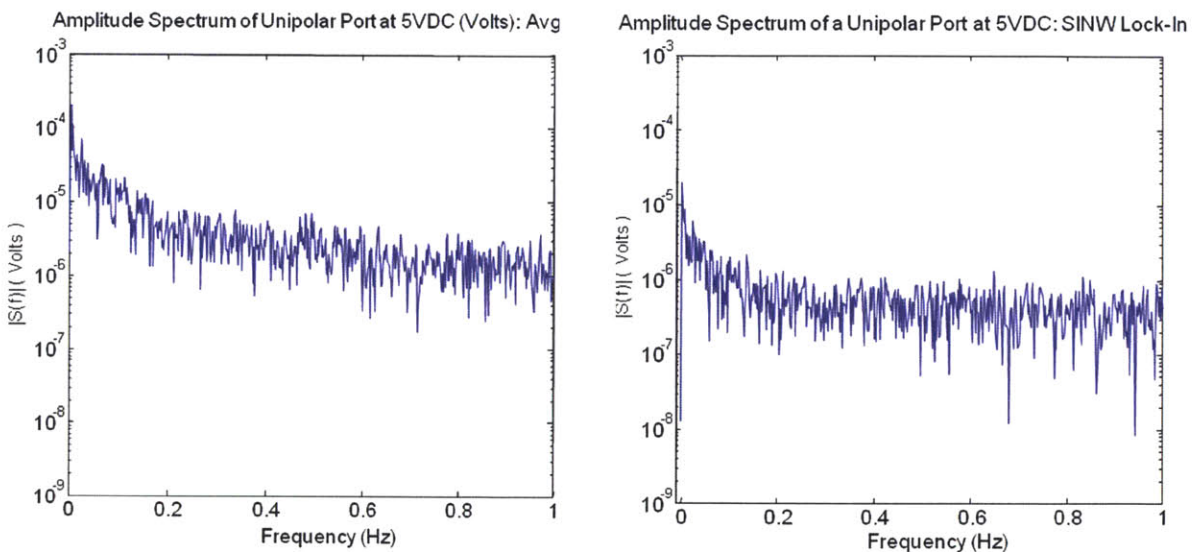
Figure 15: Low frequency FFT spectra of 5VDC locked-in

29

Finally, a 20 Hz sinusoid was supplied by an external function generator and modulated by a 10 kHz reference frequency through use of the circuit shown in Figure 8. As in the previous tests, the circuit's output signal was then delivered to the acquisition system and the sin(ω) lock-in data recorded to verify the manufacturer's signal-to-noise ratio. The resulting FFT is displayed in Figure 16.
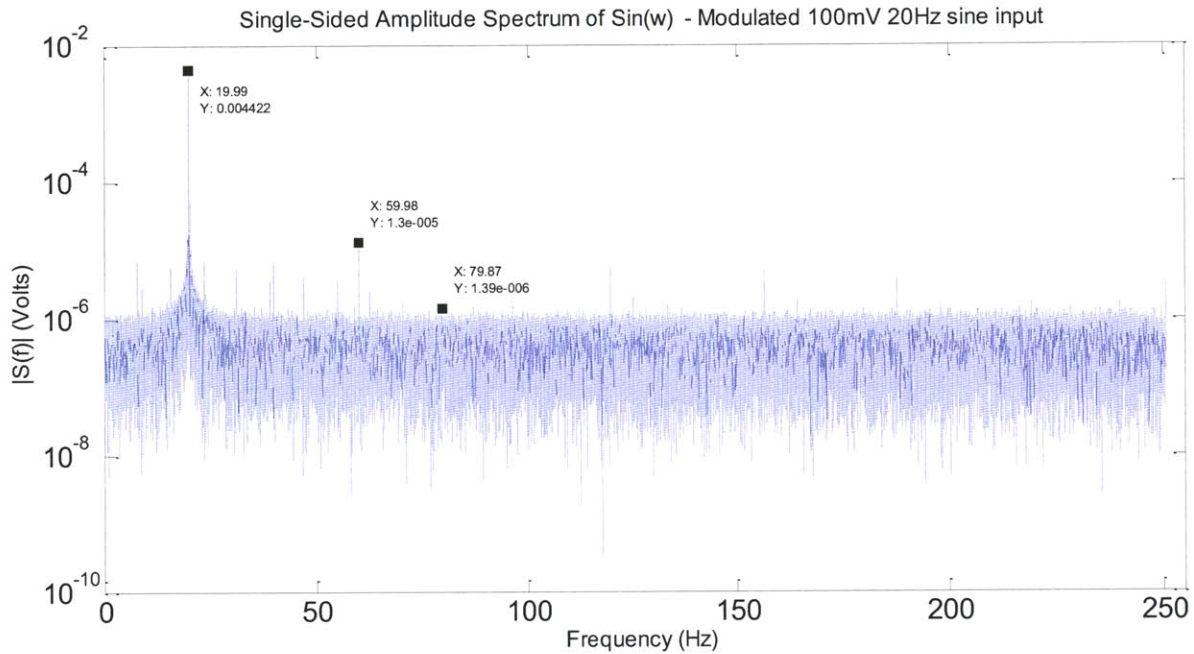
Figure 16: FFT spectrum of 20Hz sinusoid locked-in

Due to limitations in the circuit, a maximum of 250mV$_{PP}$ sinusoid could be modulated by the circuit and delivered to the data acquisition system. Regardless, the maximum noise source at 60Hz is intrinsic to the electronics and should not scale as the amplitude of the sinusoid is increased to its maximum input value of 20V$_{PP}$ (given the input range of $\pm$10V). The SNR can still be estimated by multiplying the 20Hz peak amplitude by 80 to simulate the full-scale voltage and using the maximum noise peak at 60Hz.

$$SNR = 20\log\left(\frac{Full\ \ Scale\ \ Signal}{Maximum\ Noise}\right) = 20\log\left(\frac{.004422 \times 80}{1.3 \times 10^{-5}}\right) = 88.7dB$$

This signal to noise ratio is actually slightly better than the manufacturer's specification sheet due to our custom hardware lock-in amplifiers. Another fact to consider is that the SNR can actually be increased further if the source of the 60Hz noise and its harmonics can be eliminated so the maximum noise level approaches the noise floor of about 1.4×10^{-6} Volts.

2.3 Analog Output Hardware

The full 64 sensor magnetometer system requires a total of twenty-one independent analog outputs. These include the modulation signal used for lock-in amplification, 18 outputs to control the magnetic coils surrounding the sensor, and two outputs that can be used to modulate the lasers. The modulation output is supplied by the acquisition card due to the same signal being used for lock-in processing. The remainder of the outputs is provided by an analog output card also designed by D-tacq (part number AO32CPCI). This card was chosen for its flexibility as well as its compatibility with the custom acquisition system. It mounts in the same chassis as the acquisition board which allows communication over the same Ethernet line. The board provides a total of 32 analog outputs with a range of ±10 Volts and is controlled by commands sent from the PC. While timing for the coil and laser analog output waveforms will be controlled by the AO board's internal clock, the common chassis mount allows for clock sharing between the acquisition board and the analog out board. This provides potential for additional lock-in processing using the AO board outputs in the future. Twelve analog outputs also remain unused in the current sensing system and can provide additional functionality in the future.

2.4 Acquisition Hardware Summary

After full testing and validation it appears that the acquisition system with the additional analog output control surpasses the necessary requirements for the full 64 sensor array and provides great options for future scalability. The full acquisition system's verified specifications are shown in Figure 17:

Acquisition System Input	
Inputs	96 Channels (Ch 1-64 ±10V floating input) (Ch 65-96 0-10V floating input)
Lock-in Amplification	5-way referencing (Ch 1-64) 1-way referencing (Ch 65-96)
Noise Floor (inputs shorted)	139 dB
Signal-to-Noise Ratio	88.7 dB (estimated, with full-scale input)
Maximum Throughput	1,671 Hz (all references enabled) 6,266 Hz (one reference per channel enabled)
Analog Outputs	
Outputs	32 Analog Out Channels (±10V, 10mA max) 64* Digital Out Channels (*untested/unused)

Figure 17: Acquisition System Verified Specifications

Chapter 3 – Digital Signal Handling and Processing

3.1 Signal Handling

After much consideration, Draper's own custom software package called Draper Simulation Framework (DSF) was chosen for digital signal handling of the SERF sensor array. DSF has the ability to handle data acquisition, system control and signal handling tasks while allowing for real-time data processing. The software package has a modular architecture that consists of individual application-specific modules that can be designed to control system functions. This modular architecture allows changes to or additions of specific system functions without modifying other aspects of the system control and design. This is a very versatile software design that provides great flexibility and scalability. As new components are added to a system, a new DSF module can be built and added to the software package. DSF modules can also be written in basic programming languages such as C++ or compiled through other software such as The Mathworks' Simulink. For the work described in this thesis, the hardware running DSF consists of a standard Dell desktop PC running Red Hat Linux (enterprise version 5.2). A block diagram of the overall system architecture can be seen in Figure 18.
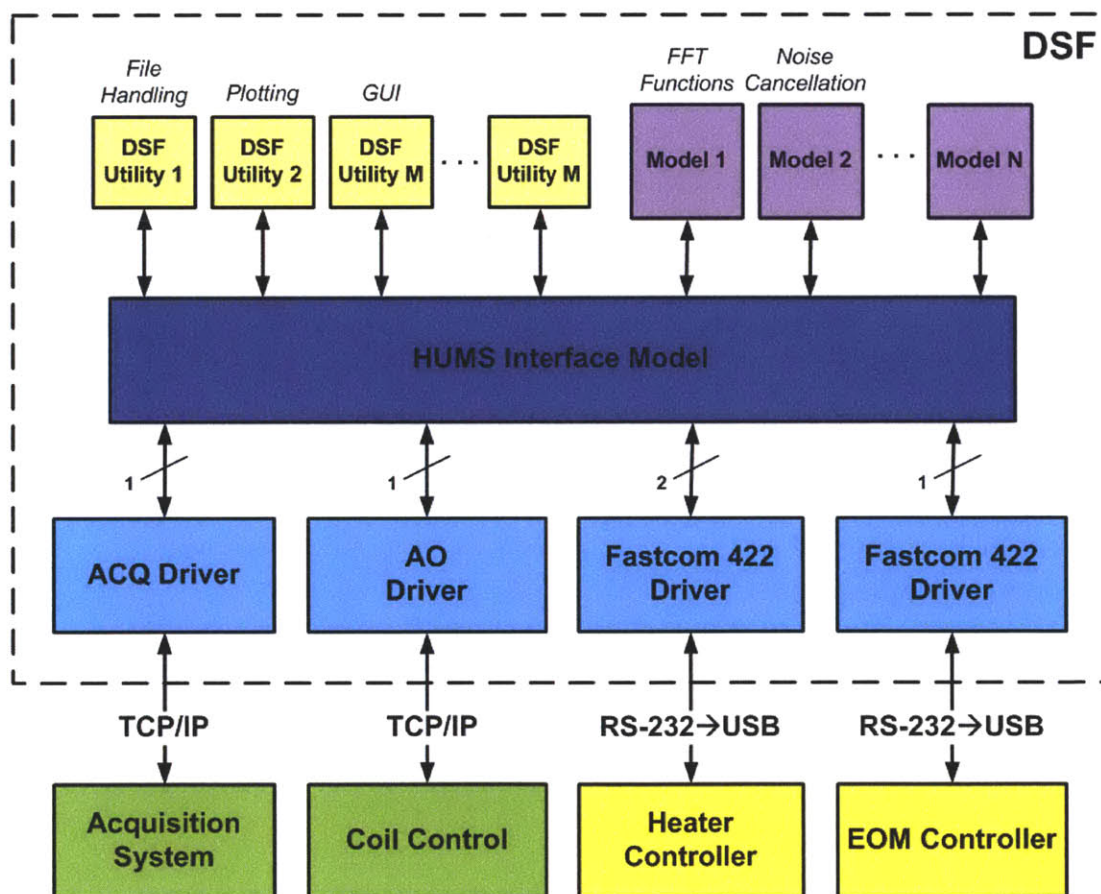
Figure 18: DSF System Functional Block Diagram

In Figure 18, everything contained within the dashed box is part of the custom Draper Simulation Framework package being developed for this application. The HUMS interface model is the main software component that accesses and controls all other DSF models, utilities, and hardware drivers. The software models are typically used for different forms of data processing and routing within DSF. Utilities are additional software packages designed to give DSF additional functionality, such as improved plotting or supplying a custom graphical user interface (GUI). Hardware drivers handle communication between the PC and additional hardware such as the acquisition board or the heater controller. This module-based system allows for great flexibility in the system design. If additional functionality is desired or certain models need modification it can be performed with no effect on other aspects of the software.

As mentioned previously, DSF is also responsible for handling the large amount of data from the acquisition system. Due to the sheer volume of data coming from the acquisition cards, the acquisition card packages the data in a "frame" structure before sending it to the PC via Ethernet. This reduces the chance of data loss and allows for the Ethernet lines to be less taxed than if data was streamed continuously. This packaged data needs to be sorted and mapped to each respective channel and lock-in reference before any post-processing can be performed. The format of the data packets is shown below.
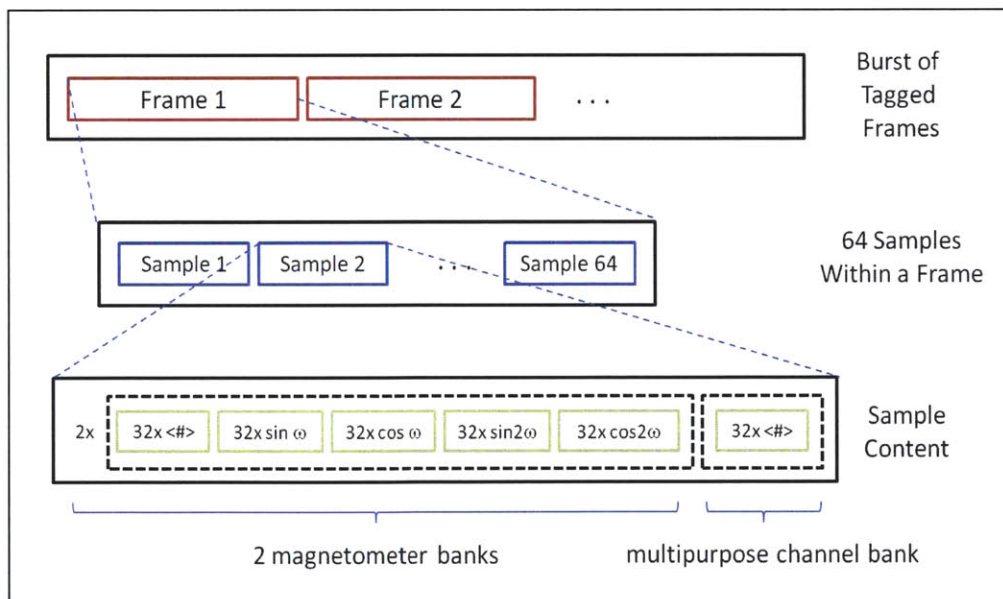
Figure 19: Acquisition System Data Packaging

Each frame contains 64 samples, or measurements performed by all channels' lock-in references at the same point in time. Within each sample, data is further organized by structuring the data into individual banks of 32 channels. Each bank contains the lock-in reference data for all 32 channels. For

example, if all five lock-in references were enabled on the first channel bank there would be $32 \times 5 = 160$ individual data points in that bank. For our specific application, the first two channel banks are used to acquire data for the 64-sensor magnetometer array and have all five lock-in references enabled. Therefore, each of the two magnetometer banks contains five data points for each channel, representing the demodulated data per the {DC, $\sin(\omega)$, $\cos(\omega)$, $\sin(2\omega)$, $\cos(2\omega)$} reference scheme. The third channel bank is not currently in use and has only the DC reference enabled. This third bank can be used for additional equipment monitoring such as temperature or laser performance in the future. The entire transmitted data stream is unwrapped and mapped to the respective channel and reference in the DSF HUMS interface module. The data is then logged and plotted in real-time using the existing file handling and plotting utilities in DSF. The raw data can also be scaled to produce voltage readings through the HUMS interface model.

The Draper Simulation Framework software package is also responsible for all digital post-processing performed on the data, including adjustable filtering and FFT processing as well as system control tasks such as temperature control and EOM offset control. The Fourier transform and digital filtering of the data is performed by custom developed DSF models on the host PC.

3.2 Fast Fourier Transform Model

The fast Fourier transform is used to convert data from the time domain to the frequency domain and is one of the most useful tools for determining magnetometer performance. Having the ability to plot real-time FFTs allows the operator to view the frequency components of the output signal during active measurements. Sources of noise can then be observed and potentially removed to improve overall sensor performance. For example, while performing initial sensor testing at Draper Laboratory relatively large $1/f$ noise was observed. The system response was monitored as individual pieces of equipment were powered off and on. The FFT showed that a large part of the noise was removed when an amplifier supporting the electro-optic modulator was powered off. It was deduced that the amplifier was the source of the noise and it was replaced by a similar one. Further testing revealed that sensor performance was improved with the new amplifier. If noise cannot be mitigated by hardware changes, the FFT can also be useful to determine the best digital filter design to post-process the data.

The FFT is also used to determine the ultimate sensitivity of the SERF sensor head. A known magnetic field at a modulation frequency (such as 5 Hz) is applied to the sensor head using external magnetic coils. The amplitude is slowly reduced until the modulation frequency spike on the FFT can no longer be discerned from the background noise. The magnetic field amplitude at this point is the ultimate sensitivity of the sensor head at this modulation frequency and at this bandwidth (more sophisticated

signal vs. noise criteria can be employed as well). With further lowpass filtering the SNR should improve. This sensitivity can be measured for a broad range of modulation frequencies to determine overall sensor performance.

As mentioned previously, one of the benefits of the Draper Simulation Framework is that it provides compatibility with some third party software, such as the Mathworks' Simulink. Simulink is a block-based programming tool designed for simulating and analyzing dynamic systems. It is a well-designed and simple tool for signal handling and processing and the graphical programming allows for easy visualization of data flow. Through the use of Simulink's Real-Time Workshop, the block diagram 'code' can be compiled into stand-alone C code which then acts as a model in DSF. Because of this simplicity and flexibility, Simulink was used to develop the fast Fourier transform (FFT) data processing model. The final model can be seen in Figure 20.
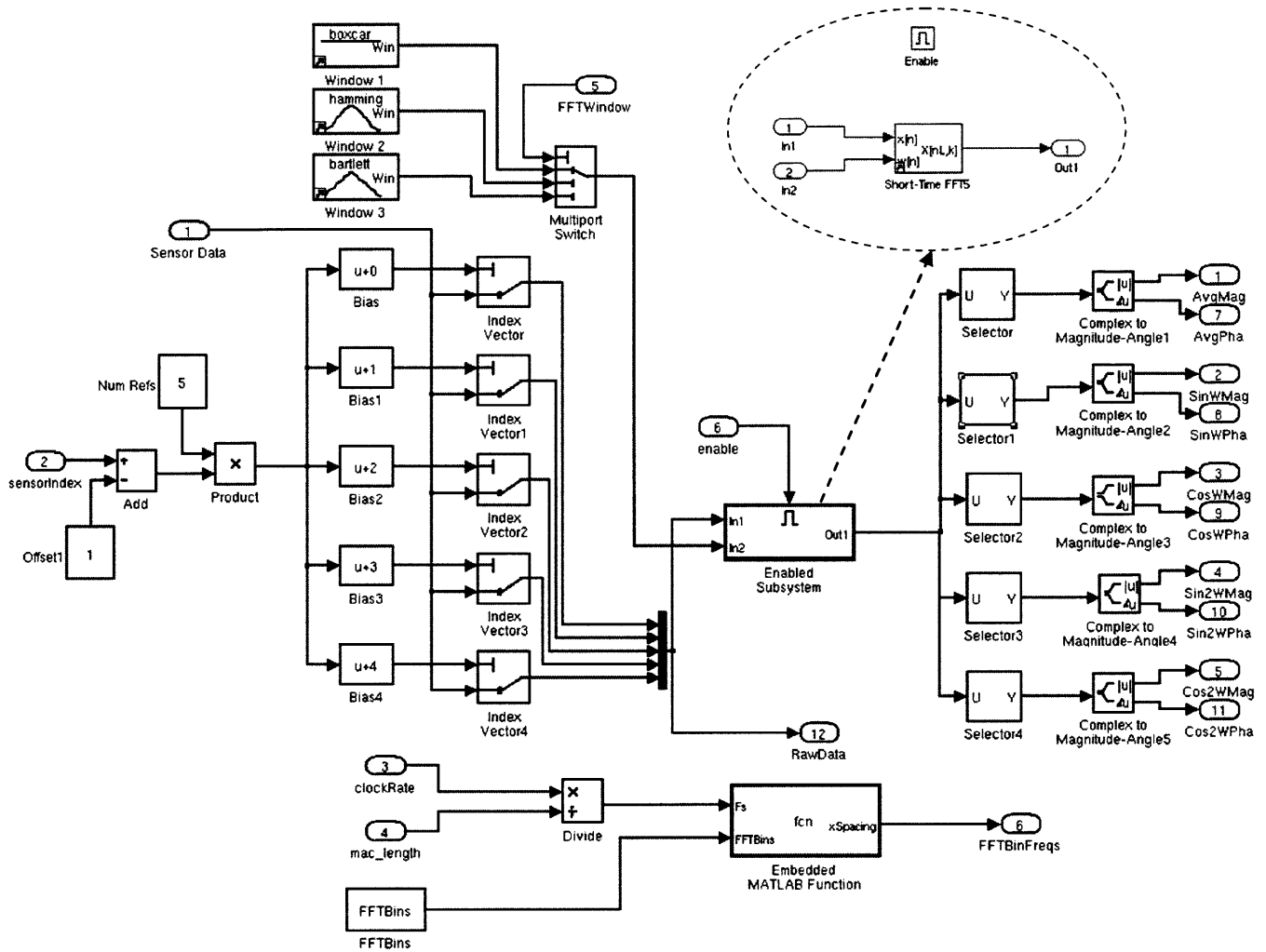
Figure 20: Fast Fourier Transform Simulink Model

This model is designed to perform an FFT on a single channel from the acquisition system. All external inputs and outputs (which are displayed as numbered ovals in the diagram) are supplied by the DSF HUMS interface model. Rectangular elements in the model represent Simulink data processing functions. The model first reads the user's desired channel via the *sensorIndex* block and inputs all raw data from the acquisition system via the *Sensor Data* block. The *Bias* blocks then parse the framed data (see Figure 19) into the five individual lock-in references (DC, sin(ω), cos(ω), sin(2ω), and cos(2ω)). This data is then combined into a single stream which is provided to an external output for datalogging as well as analysis by the FFT routine (which can be windowed depending on the user's preference, although a Hamming or Bartlett window will typically be used to remove DC signal). The short-time FFT block buffers 512 points of the input data, overlaps it with 384 points from the previous window, applies the windowing function, and zero pads the signal to 1024 points. It then computes a nonparametric estimate of the spectrum using the standard Matlab FFT routine. The multiplexed stream is then split back into

36

individual lock-in references and the magnitude and phase from the FFT provided as an output for each. The FFT processing can also be disabled by an external input to reduce computing overhead if the user does not want FFT processing. The time domain to frequency scaling is also performed by a separate embedded Matlab function.

3.3 Digital Filtering Model

Digital filtering is a useful tool for removing noise from the sensor output that cannot be improved through hardware changes or lock-in demodulation. Digital processing allows for real-time changes and provides much greater flexibility in design than analog filtering. Digital filtering also provides much better control of accuracy requirements as filter hardware tolerances do not play a factor in design. In addition, the filter can simply be switched on or off for debugging purposes through the host PC. For these reasons a digital filtering model was also designed and implemented in DSF via Simulink.
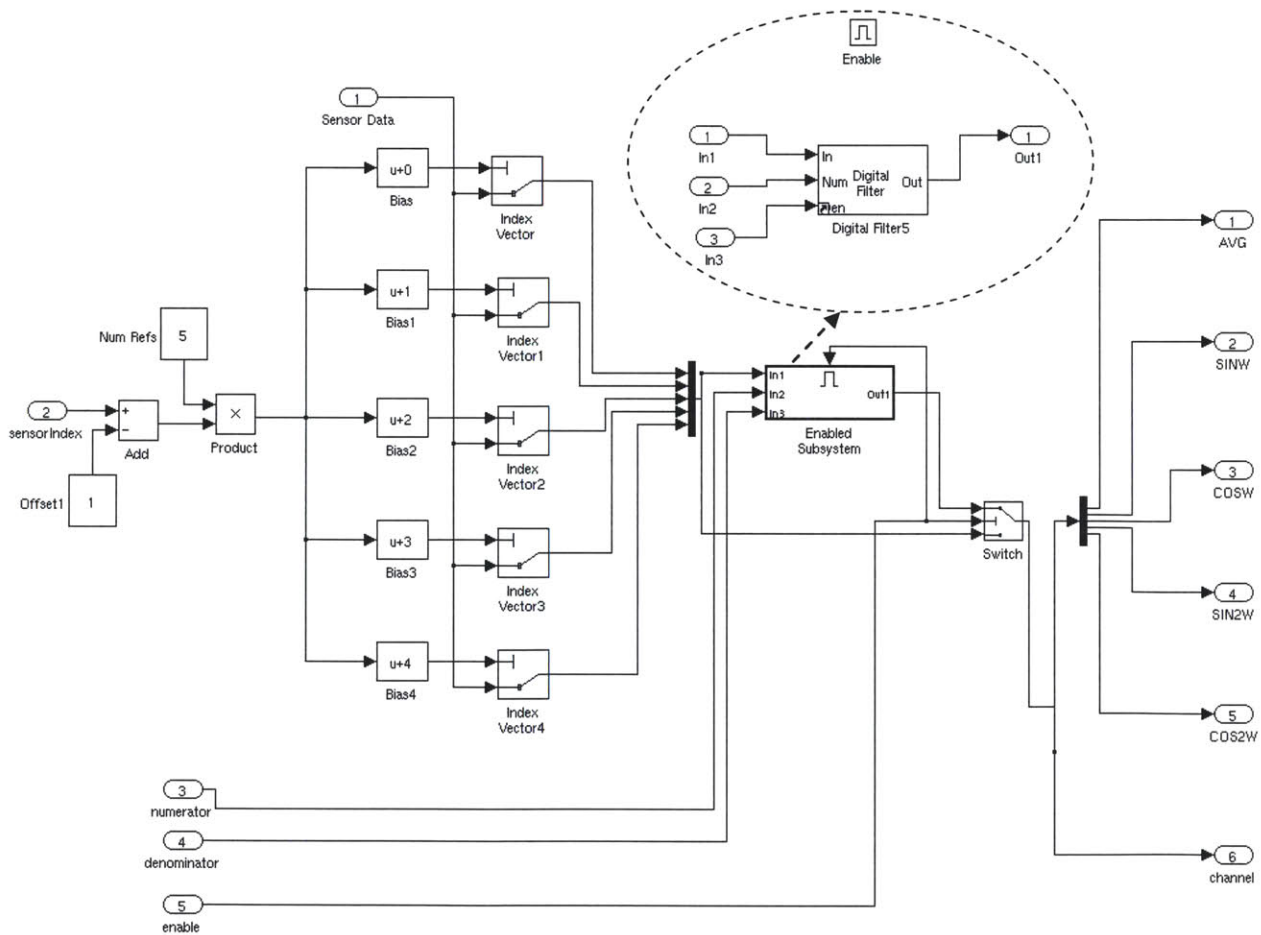
Figure 21: Digital Filtering Simulink Model

The filtering model is very similar to the FFT model in structure and design (see Figure 21). The model is designed to filter data for a single channel as well as provide an output for the raw pre-filtered data. The data stream is parsed to pull the desired channel's raw data. This data is then separated into individual lock-in references and multiplexed through a fully customizable digital filter which is defined by user-input z-transform coefficients. Default filter designs are provided via the HUMS interface model but the user is also able to input his or her own design. Additionally, the digital filter block can be disabled and bypassed to save computing resources.

Chapter 4 – User Interface

4.1 Background

A custom graphical user interface (GUI) was developed using Qt4 (a GUI development package) and integrated as a DSF model. The GUI serves as the main connection between the end user and sensing system hardware and software control. All acquisition and system control is done through this fully custom user interface. The user can control the heater, magnetic coils, and electro-optic modulator driver through the software, as well as control and monitor the data acquisition system and the software-based signal handling and processing

Draper's Human Use Engineering Group was consulted during the design process to ensure simple and intuitive control. Care was taken to ensure that all information is displayed clearly and can be easily understood by the end user to ensure smooth operation and allow for quick diagnosis and correction of any equipment problems. A "tabbed" GUI design, similar to most internet browsers, was chosen to allow quick access to the different controls while not consuming the limited screen real estate. Important notifications and warnings are always displayed on the bottom of the screen, regardless of the current tab. Colors are used to allow quick status verification; any errors or problems typically result in a red indicator on screen. Finally, plotting of the sensor measurements was developed as an independent window to allow for easy interpretation of system input changes on sensor output and performance. Additional discussion of GUI design and function is provided in Section 4.3.

4.2 Hardware Interaction

The graphical user interface serves as the portal between the user and the full sensing system (see Figure 18). It must therefore interact with the different hardware components through DSF models that directly communicate with the external hardware. These custom DSF models are each built to take the user input and translate it into commands understood by the hardware. Each piece of hardware has its own tab on the GUI to allow for simple and intuitive control.
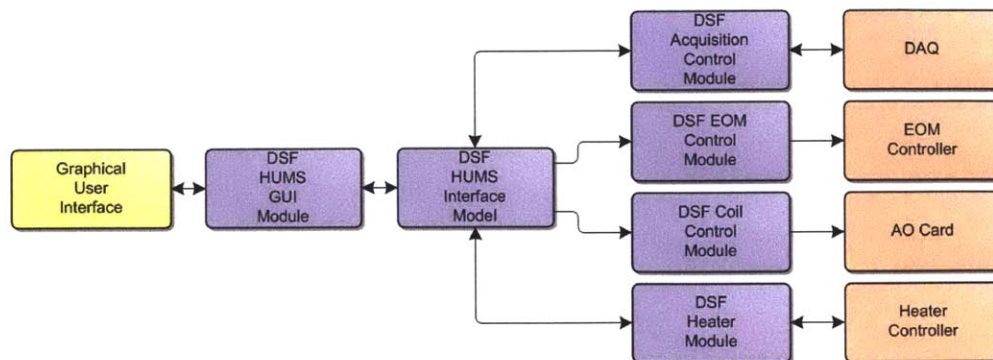
Figure 22: GUI to Hardware Control

39

4.3 GUI Controls
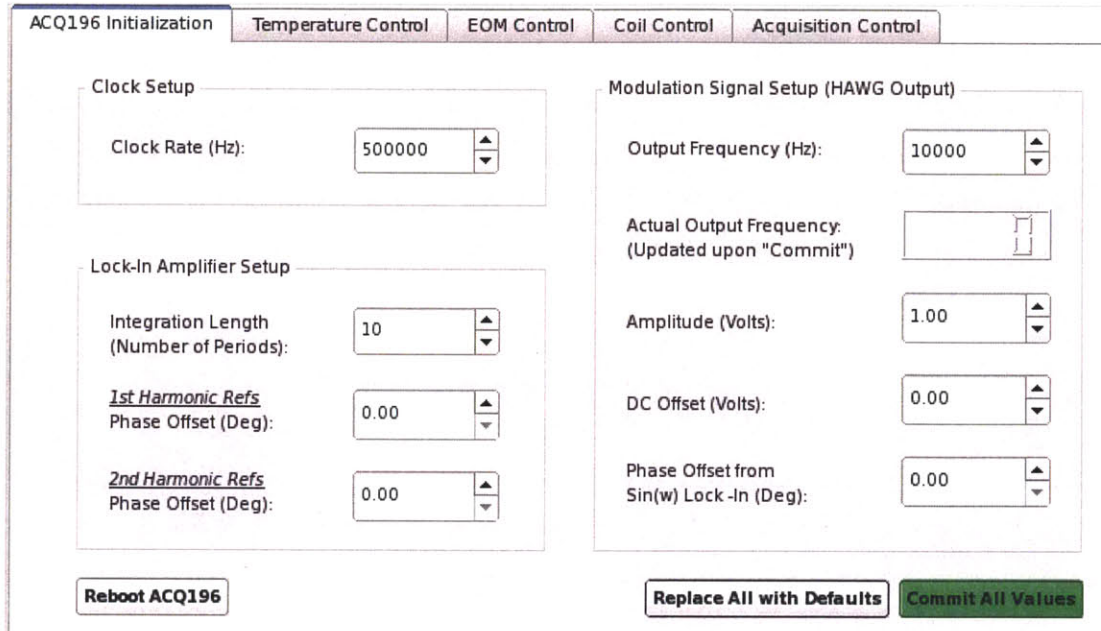
Figure 23: GUI Initialization Tab

The tabs of the GUI are placed in an order they would typically be accessed while setting up the sensors and performing a measurement. The first tab visible to the user is the initialization tab (see Figure 23). It is used for the initial setup of acquisition system. The acquisition rate, lock-in amplifier integration length and phase offset, and output modulation frequency can all be adjusted via these controls. The output frequency is also hardware limited due to the fact the signal is generated digitally. The modulation output frequency must be equal to 66MHz/N, where N is an integer, due to the acquisition card's internal clock. The GUI reads the user's desired modulation frequency and calculates the closest possible frequency the hardware can generate. This value is displayed in a widget as well as sent to the acquisition card via the "commit" button. There is also a "reboot" button for use if the acquisition hardware malfunctions and becomes unresponsive. Once the acquisition card is initialized via the "commit" button these settings will typically be left untouched for all further system tests and measurements.
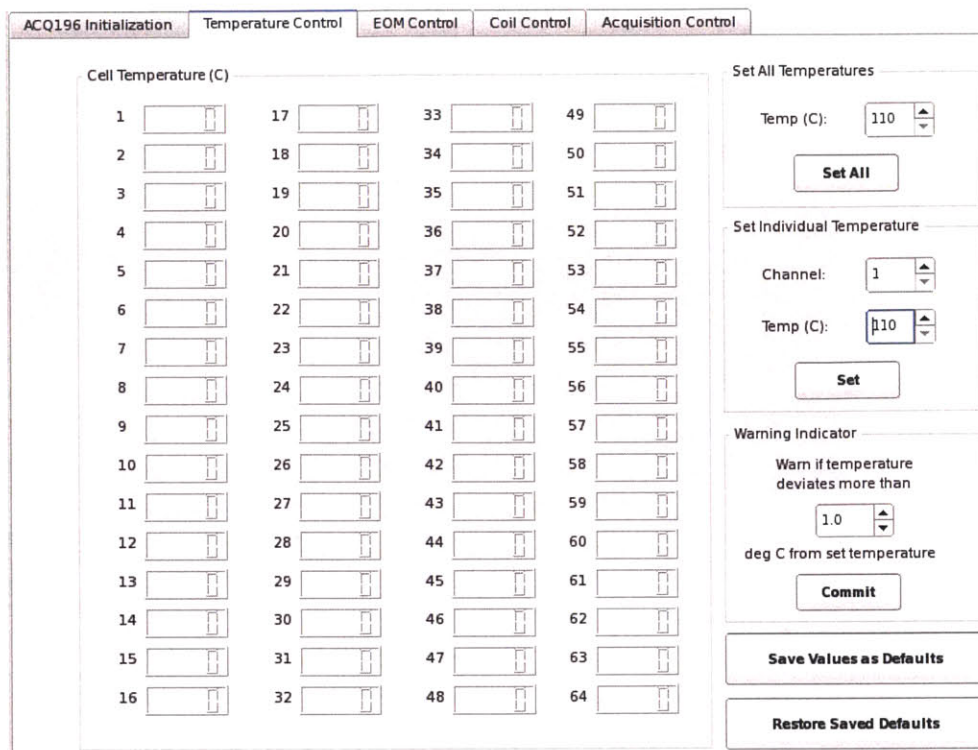
Figure 24: GUI Temperature Control Tab

The following tab controls the temperature of all 64 cells in the sensing array. As mentioned in Section 1.3, optimal sensor performance occurs at elevated temperatures which increase the vapor pressure in the glass cell. Due to the fact that the sensors are hand-assembled there are slight variations in the optical alignment and vapor cell placement relative to the heater pad within each sensor. Individual temperature control allows the user to "balance" all cells so they respond similarly. The temperature also directly affects the performance of each sensor and should be easily monitored and changed if necessary. The GUI layout allows the user to view the current temperature of all 64 sensors at a glance. A single "set temperature" control is used instead of 64 individual controls to reduce clutter and allow for quick temperature reading.

There is a "set all" button that allows the user to initially set all 64 temperatures to the same temperature to view the sensors' response before fine-tuning temperature (if necessary). A warning option turns the temperature indicator for each sensor bright red if the temperature deviates by more than a user-specified value from the desired set temperatures. There is also a general temperature warning indicator visible from all tabs that becomes red if any sensor deviates by more than the specified amount (see bottom of Figure 26). Finally, the "save value" and "restore value" buttons allow the user to save the current temperatures in a file for future use and should allow the user to skip the potentially tedious individual temperature balancing step for future measurements (assuming the same sensing array operated

undet the same conditions is used). Once the temperatures are balanced and stable, this tab generally requires minimum user attention.
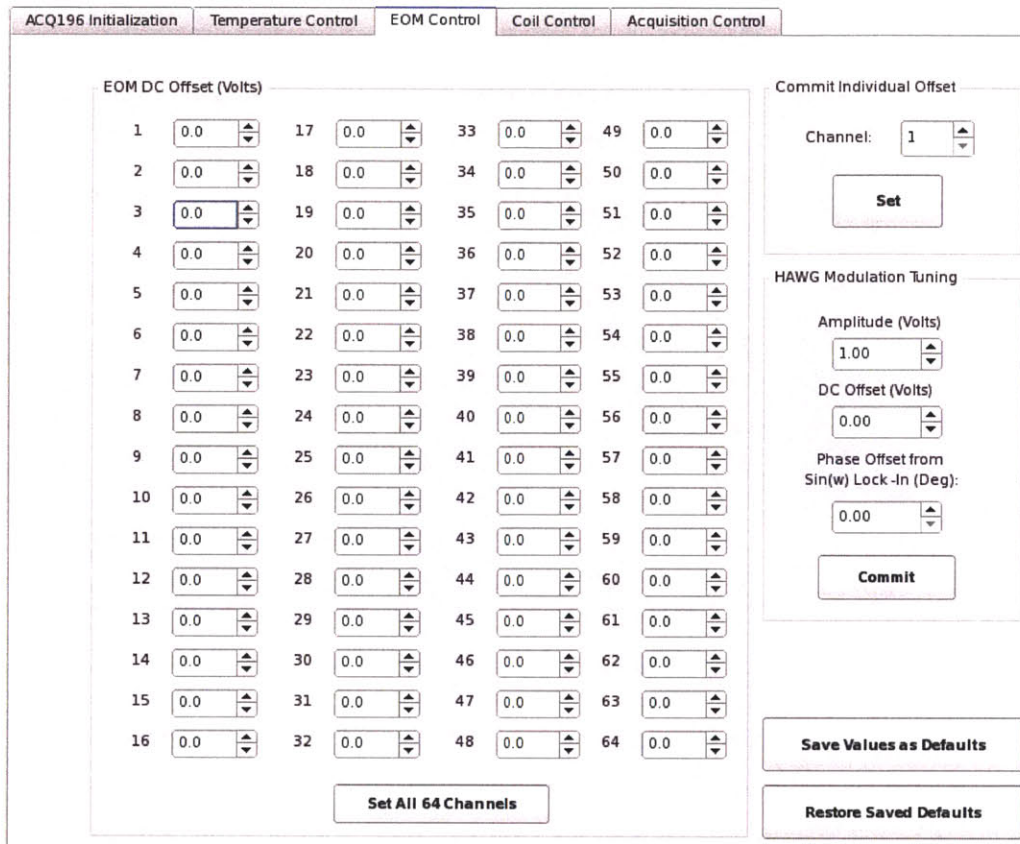
Figure 25: GUI Electro-Optic Modulator Control Tab

Once the temperatures of the cells stabilize, the user tunes the electro-optic modulator (EOM) for each sensor. The user must wait for the temperature to stabilize because the EOM crystal properties change with temperature. The GUI reads the user's input and sends out the necessary commands to the EOM control board to set the DC voltage offset for each channel, which changes the probe beam's polarization angle (see Section 5.3 for more detail). The EOM control tab itself is very similar to the temperature control tab, as each sensor can be independently adjusted. However, the DC offset is hardware controlled and should not fluctuate, so no voltage offset polling and display is necessary on the GUI. The layout allows the user to quickly view the set DC offset for each sensor's EOM driver at a glance. A "set all" button is included for convenience and sends commands to all 64 EOM control boards. To reduce lag and computer overhead a single channel "set" button is also available to the user. Similar to the temperature controls, save and restore buttons are available to reduce setup and calibration time for future runs.

42

As seen in the system diagram (see Figure 5) the modulation signal is sent to each EOM control board before being amplified and sent to all 64 sensors. The EOM amplifier board takes this common mode signal, amplifies it, and then adjusts the DC voltage offset for each channel. For this reason, modulation signal fine-tuning controls are also presented to the user on the EOM control tab. This allows the user to adjust all aspects of the EOM on one page.
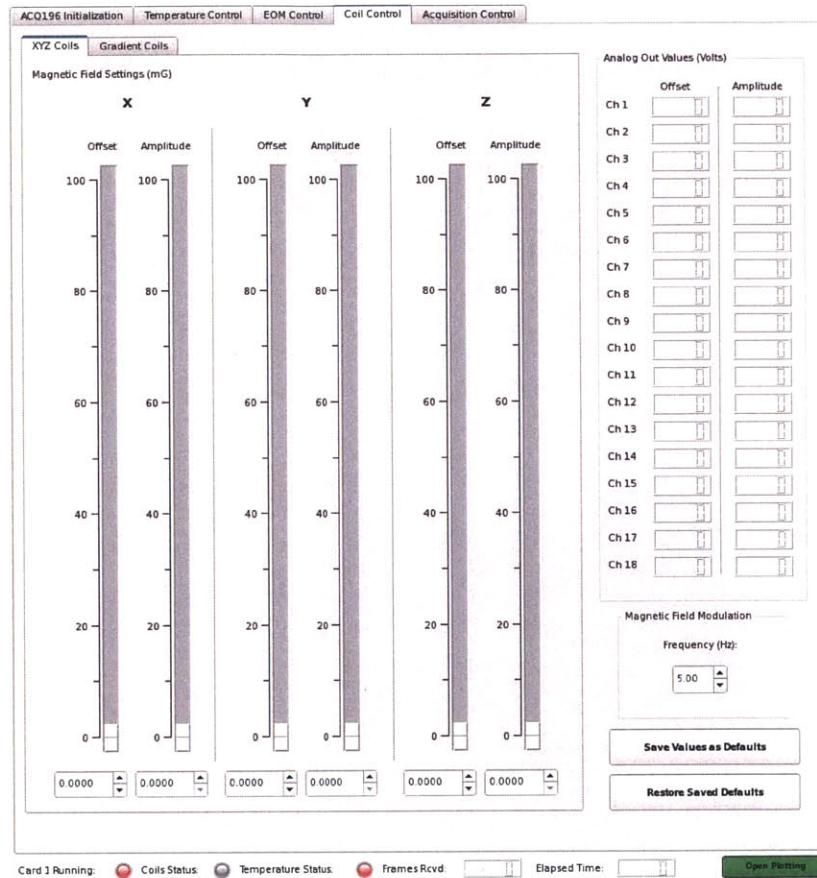
Figure 26: GUI Coil Control Tab

The fourth GUI tab (see Figure 26) addresses the need for magnetic field control via magnetic coils built into the magnetic shield that surrounds the sensing array. They are used to null the effects of the earth's magnetic field as well as modulate an applied magnetic field to determine the sensor's sensitivity. There are two configurations of shields and magnetic coils in which the sensors are used. The first is a small magnetic shield at Draper Laboratory that contains three magnetic coils and was used for preliminary testing. These coils directly control the magnetic field in the X, Y, and Z direction. The second magnetic shield is located at Princeton University and will be used for the testing of the full 64 sensor array. This shield contains 18 magnetic coils that allows for control of magnetic gradients as well as uni-directional fields. The GUI reads the user's input and determines the necessary voltages and DC

offsets for each coil to obtain the desired magnetic field. The interface also allows for simple switching between the two configurations.

Output amplitudes and DC offset voltages are also displayed for debugging purposes in the 18 coil configuration. All magnetic fields can also be modulated to provide further sensor testing. The sensor's bandwidth and sensitivity at different frequencies can be determined by applying known modulated magnetic fields. Finally, as in the other tabs, there is a "save values" and "restore values" option. The notifications visible from all tabs (on the bottom of the GUI) can also be seen in this screenshot.
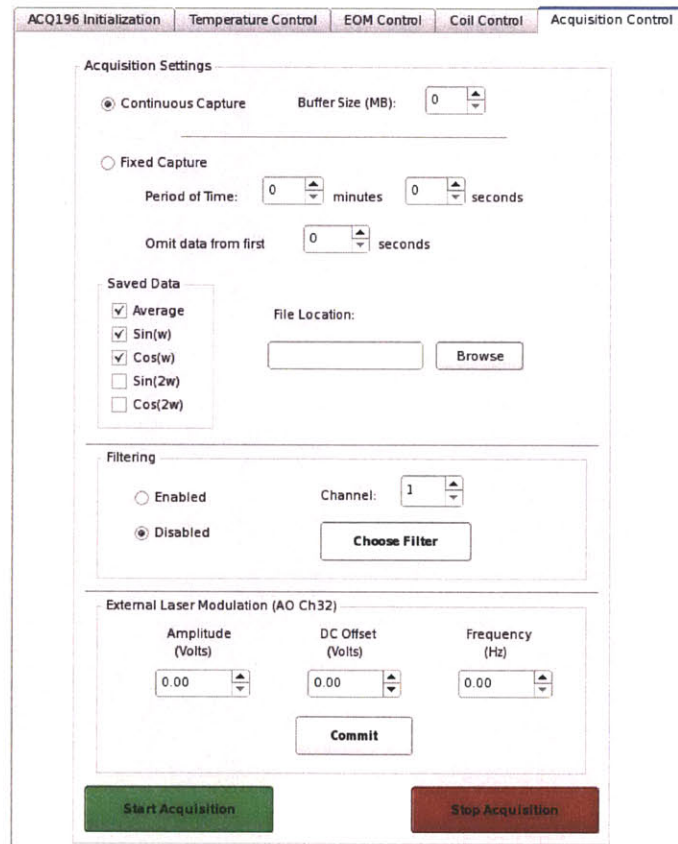
Figure 27: GUI Acquisition Control Tab

The final control tab (see Figure 27) contains acquisition settings, post-processing digital filter options, and an additional analog output control that can be used for laser modulation (provided the laser supports modulation via an external signal). From this tab the user can select which lock-in outputs and how much data to save to the hard-drive (which can be post-processed in Matlab or another mathematical analysis package). This helps save disk space and computational overhead due to the massive amounts of data coming in. There is also a filtering option that allows the user to post-process a select channel in real-time with either a pre-configured filter or a filter of his or her own design (specified through the z-

transform coefficients). Filtering can be disabled to further reduce computational overhead. Finally, the user starts and stops all measurement runs via this tab.
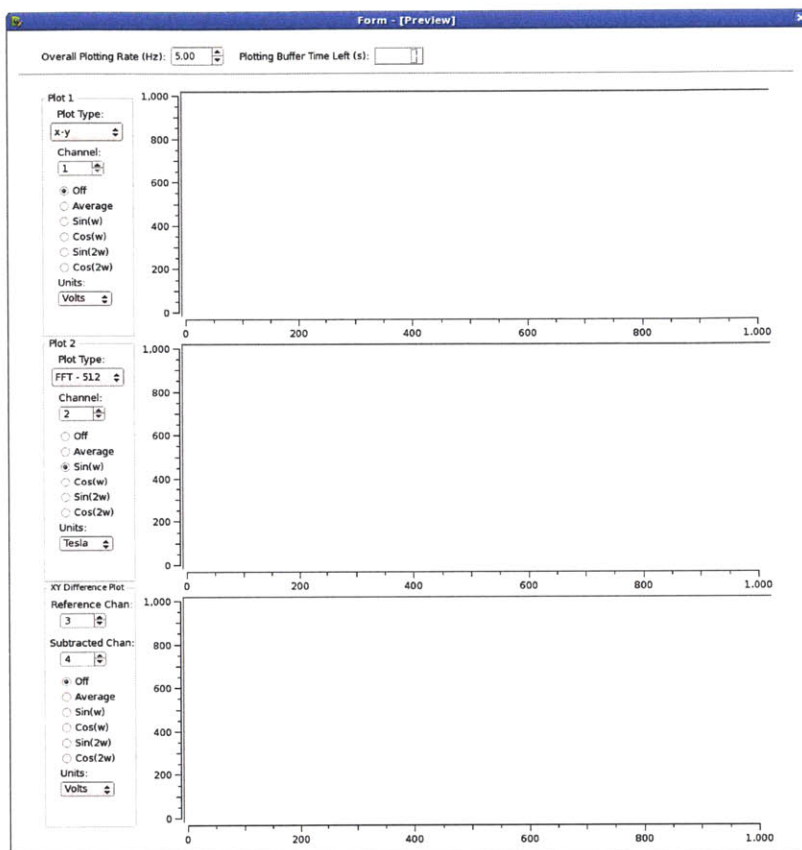
Figure 28: GUI Plotting Window

The plotting window (see Figure 28) is separate from the control window, allowing the user to directly correlate changes in sensor settings to their measured output (with this configuration the user can make full use of the PC's dual monitors by leaving one window maximized on each screen). The plotting interface was designed for flexibility and allows the user to view the sensor's output in a variety of ways. The first two plots can be used for any sensor and lock-in reference in the array and are capable of displaying the time-varying voltage output from the acquisition system or the fast Fourier transform (FFT) of the output. The third plot displays the output difference between any two sensors in the array. This is very useful for either finding errors/inconsistencies in the magnetic field as well as making gradiometric measurements using two sensors. As in many other aspects of the sensor control, individual plots can also be shut off to save computing resources. Regardless of the plotting settings, all user-specified sensor output data is saved to a data file that can be analyzed and post-processed outside of the Draper Simulation Framework.

45

4.4 Conclusion

The custom user interface designed for use with a SERF magnetometer sensing array was developed in Qt4 and integrated into the Draper Simulation Framework control and simulation software package. The Draper Simulation Framework serves as the backbone for the entire sensing array's hardware and software control. Besides the physical powering and adjusting of the lasers, full system control is performed through the user interface. Care was taken to ensure simple and intuitive operation and an overall good user experience. For this reason, a tabbed graphical user interface style is used to reduce on-screen clutter and group controls for all independent systems within the sensing array. The interface is also organized so the user can simply follow the tab order to initialize and perform measurements with the SERF magnetometer array. User friendly controls provide the ability to set and store default values to reduce setup time and repetitive tasks. Finally, the interface provides substantial flexibility in both viewing and post-processing the sensor array's measurement data.

Chapter 5 – Sensing System Configuration and Testing

5.1 Overview

The physical systems in the full SERF sensing array consist of six main components: The SERF sensing head is the device that actually measures the magnetic field and contains the atomic vapor cell and all supporting components. The electro-optic modulator driver controls the voltage signal supplying the EOM. The heater controller is used to monitor and set the sensing head's temperature. The optical train and photodiodes supply and read the laser signals used to make measurements in the sensing head. The magnetic shield surrounds the sensing head and greatly attenuates the earth's field. Finally, the magnetic coils further aid in nulling the earth's field and also supply magnetic modulation to the sensing head to aid in sensor performance analysis. The layout of these systems can be seen in Figure 29 and all will be discussed in more detail in this chapter.
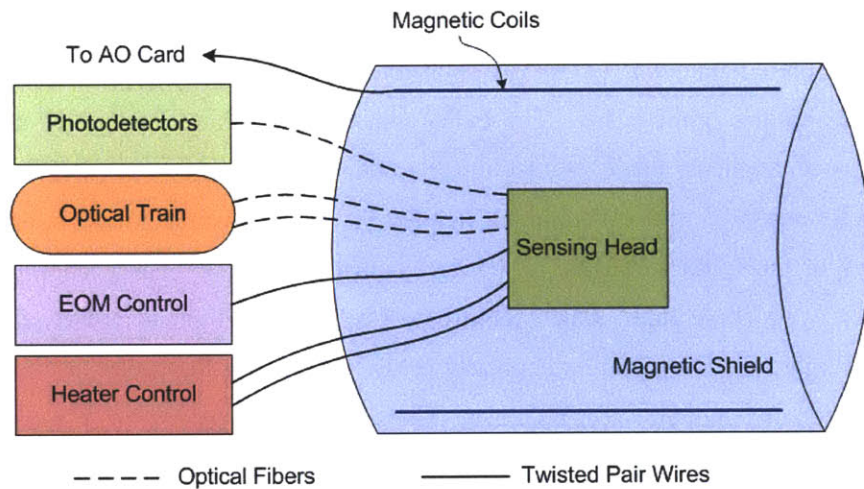
Figure 29: Physical Components in SERF Sensing System

5.2 Sensing Head

Each sensing head has a total of six connections that must be made to support sensor operation. These include three optical fibers that contain the pump beam input, the probe beam input, and the probe beam output. There are also three twisted pair electrical connections that interface with the electro-optic modulator, the thermistor (used for temperature measurement), and the cell heater. The full sensing head package includes the alkali metal vapor cell (filled with Cesium and Rubidium atoms plus buffer gasses), a prism to disperse the pump beam throughout the cell, a mirror to reflect the probe beam back into the "probe out" fiber, the heater and thermistor to heat the cell, and a structure that supports and aligns the fibers.

The pump beam is input with a polarization-maintaining optical fiber and collimated and shaped with two lenses. It is then dispersed through the vapor cell via a prism to provide optical pumping over the full cell volume. The probe beam is also input with a fiber and passes through a polarizer, a quarter wave (λ/4) plate, and the EOM before passing through the vapor cell. It is then reflected and passes back through the cell and another quarter wave (λ/4) plate before leaving the sensor through an optical fiber (see Figure 30). The heater lies on top of these components inside the package to evenly heat the entire sensing head. The entire package is enclosed in 1mm thick glass which is hand-assembled at Agiltron Inc, an optics and electronics company located in Woburn, MA (see Figure 3 for a picture of the actual sensor). To perform testing, the sensing head is placed into a foam-lined enclosure that provides thermal insulation and strain relief on the cables exiting the sensor. The final sensor head package includes an insulated Delrin enclosure which encapsulates the glass package.

5.3 Electro-Optic Modulator Hardware and Control

The electro-optic modulator (EOM) is responsible for supplying the acquisition system's lock-in modulation to the sensor's probe beam. The EOM consists of a lithium niobate crystal that changes optical properties with applied voltage. As the linearly polarized probe beam passes through the EOM it becomes elliptically polarized at the modulation frequency. The DC voltage offset is used to adjust the polarization angle of the EOM to ensure an optimal optical alignment. The probe beam then passes through a quarter wave (λ/4) plate, which removes all aspects of elliptical polarization, resulting in linearly polarized light that is oscillating angularly at the modulation frequency ω. This beam passes through the vapor cell and another linear polarizer. The second linear polarizer is placed orthogonally to the first polarizer and results in an output signal relative to the degree of optical rotation. A photodiode then converts this optical signal into a voltage that is then lock-in demodulated by the acquisition system (for more detail on the background physics see [9]).
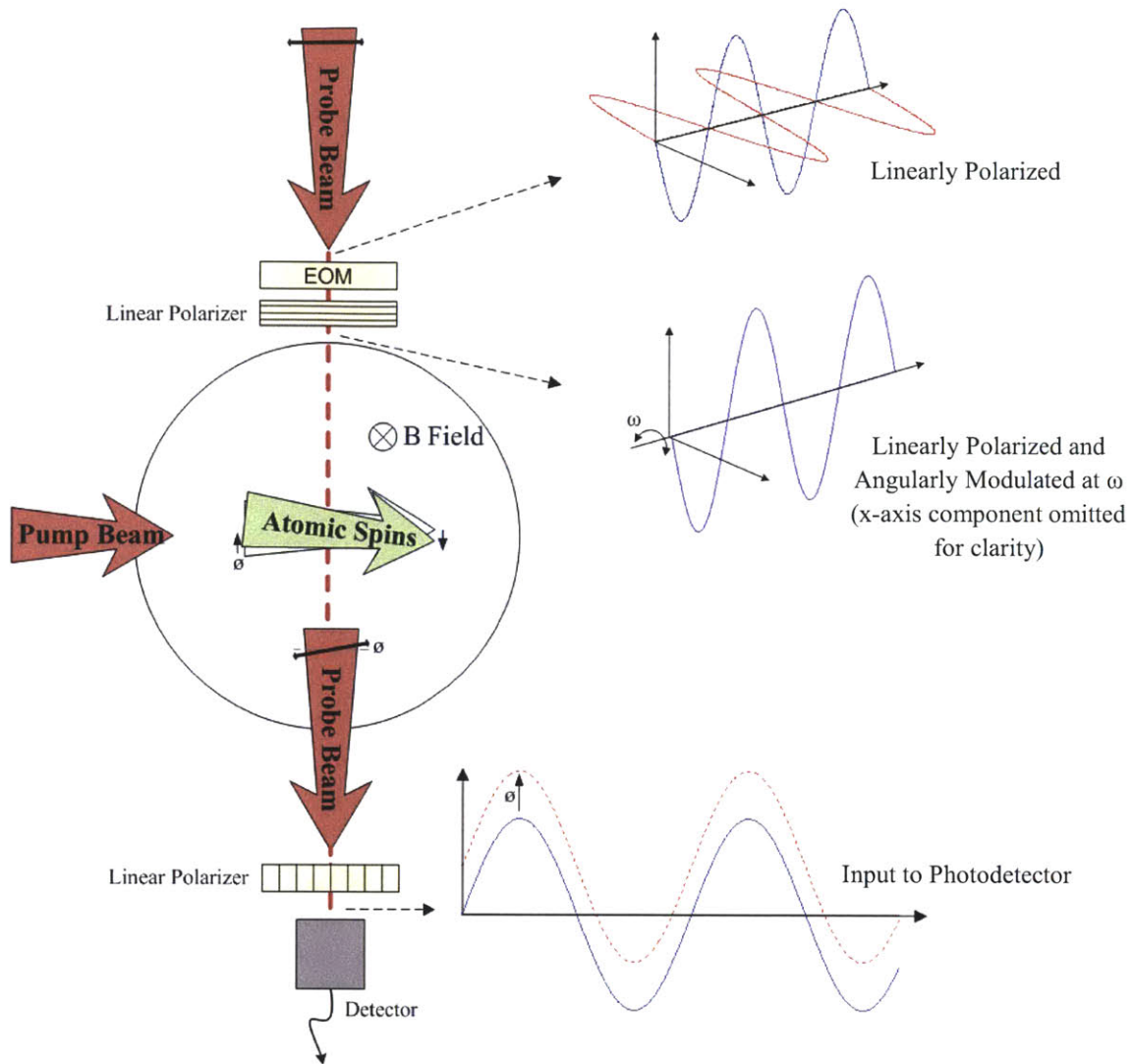
Figure 30: Electro-Optic Modulator Effect on Probe Beam

Figure 30 demonstrates the change of polarization of the probe beam on its path through the sensor and the effects of a magnetic field. The beam is linearly polarized as it enters the EOM. The EOM voltage is tuned via DC voltage offset until it elliptically polarizes the probe beam at the modulation frequency. The quarter wave plate converts the elliptical polarization into linear polarization that has a rotation angle changing at the modulation frequency ω. As the beam passes through the vapor cell, the change in atomic spin angle due to the magnetic field, ø, changes the rotation angle of the probe beam. The final linear polarizer allows for very sensitive measurement of changes in the rotation angle. The change in polarization angle from the magnetic field is picked up by the photodetector as a change in optical intensity. This results in a DC offset when demodulated by the lock-in amplifier, which is directly correlated to the strength of the magnetic field at the sensor location.

49

The hardware controlling the EOMs is designed and assembled at Agiltron Inc (Woburn, MA) and consists of an independent voltage driver for each sensor. Each custom printed control board controls 16 channels, so a total of 4 are required for the 64 sensor system. If larger sensing arrays are desired in the future the system can simply be scaled by adding more of the 16-channel driver boards. The modulation signal from the acquisition system is supplied to the EOM driver boards and is common for all channels. The driver boards amplify this signal and adjust the DC offset for each channel independently based upon user-specified input from the GUI. All communication between the PC and hardware is done through RS232 cables and communication protocol. The PC sends a command to the driver board indicating the channel number and desired DC offset. All 64 channels must be set independently. There is no feedback necessary due to the stable nature of the electronics.

5.4 Heater Hardware and Control

The heater electronics are also designed and assembled at Agiltron and the physical ceramic heater designed at Twinleaf LLC (Princeton, NJ). The final design for heater control consists of two separate components: there is a PID (proportional-integral-derivative) based heater control board for each individual sensor as well as a single printed circuit board that acts as a "switching station" between the PC and the individual heater boards. The heater control board uses pulse width modulation (PWM) at high frequencies (~10kHz) to suppress in-band current induced magnetic noise at the sensing head. A microprocessor on each control board constantly monitors and controls the sensor's temperature without any additional input from the PC. Preliminary testing of the boards was performed at Agiltron and basic compatibility with the sensor's thermistor and heater was established. Final tuning of the PID parameters and temperature control was conducted at Draper Laboratory.

All interfacing between the PC and the temperature control system is done via two RS-232 connections located on the "switching board". One connection is used to switch the individual heater board that temperature commands are sent to. The other interacts with the control board and is used to send temperature commands and read the sensor's current temperature. For initial testing a LabVIEW program was created to test both the switching speed between channels are well as actual temperature control performance (see Figure 31).
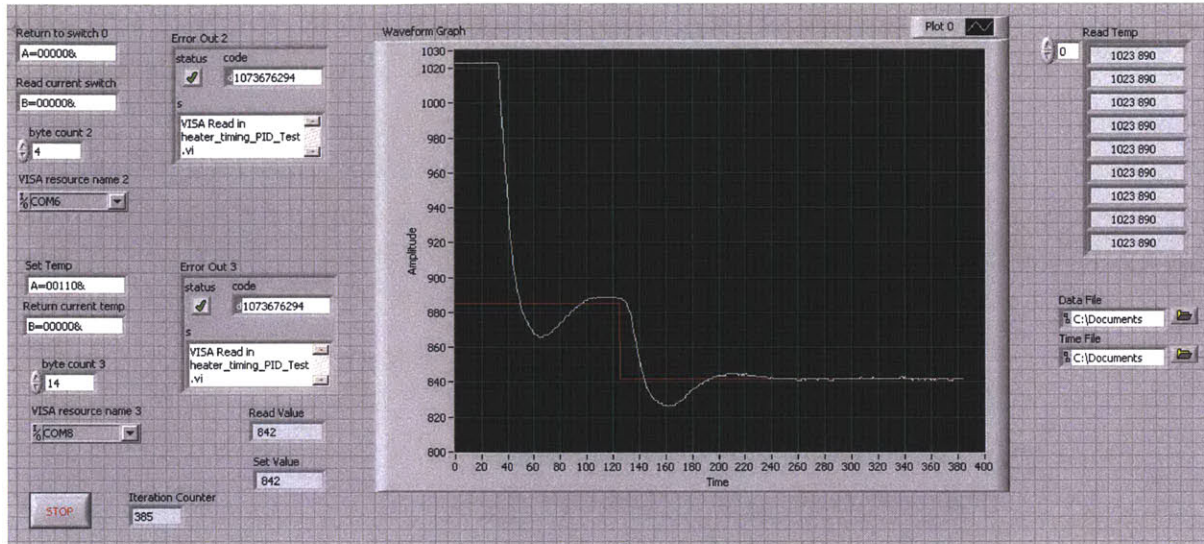
Figure 31: LabVIEW GUI used for Heater Board Testing

Initial testing revealed that the switching board can cycle through the temperature setting and reading process for all 64 channels within a time span of five seconds. This five second update rate for an individual sensor's temperature reading was deemed reasonable due to their relatively large thermal mass and the control board's autonomous nature. However, the controller performance itself was not ideal. The initial design yielded a large overshoot of approximately five degrees Celsius from the initial set temperature. Further, the controller also only allowed settings between 140-155 degrees Celsius due to limited input range of the microprocessor on the control boards (0-3V) and the choice of reference resistors used for measurement. Subsequent design iterations targeted an operating range between 110-150 degrees Celsius.

The PID settings on the controller were changed in an attempt to reduce the initial overshoot and decrease the settling time. Kiel (a division of ARM processors) μVision software version 4.0 was used to edit the controller source code with the new PID parameters and a Texas Instruments microcontroller (LM3S811 Evaluation Board) was used to flash the code onto the controller board. The controller's gain was decreased, the proportional parameter was increased, and the derivative parameter was increased to reduce the overshoot and increase temperature stability [12]. The parameters were adjusted and the controller's performance tested. This process was repeated a total of six times until the performance was deemed acceptable. The final settings had a temperature overshoot of less than 0.5 degrees and a settling time of around five minutes when set to a temperature of 110 degrees Celsius. The performance was deemed acceptable for the expected conditions under which the system will be operated.

Next, the hardware had to be modified to allow temperature settings between 110-150 degrees. The controller board uses a Wheatstone bridge to measure the resistance of the thermistor located on the

51

sensor head. The analog-to-digital converter (A/D) on the board has an input range of 0-3V. The Wheatstone bridge needed modification to assure that temperatures in the desired range resulted in voltage output between 0-3V. A SPICE (electrical circuit simulation software) model of the Wheatstone bridge was created to determine the voltage output at different temperatures. Three resistor values in the bridge were changed to shift the offset of the output and assure that the 40 degrees Celsius measurement range uses the full 3V input of the A/D.

Modified Heater Board Output (from SPICE)
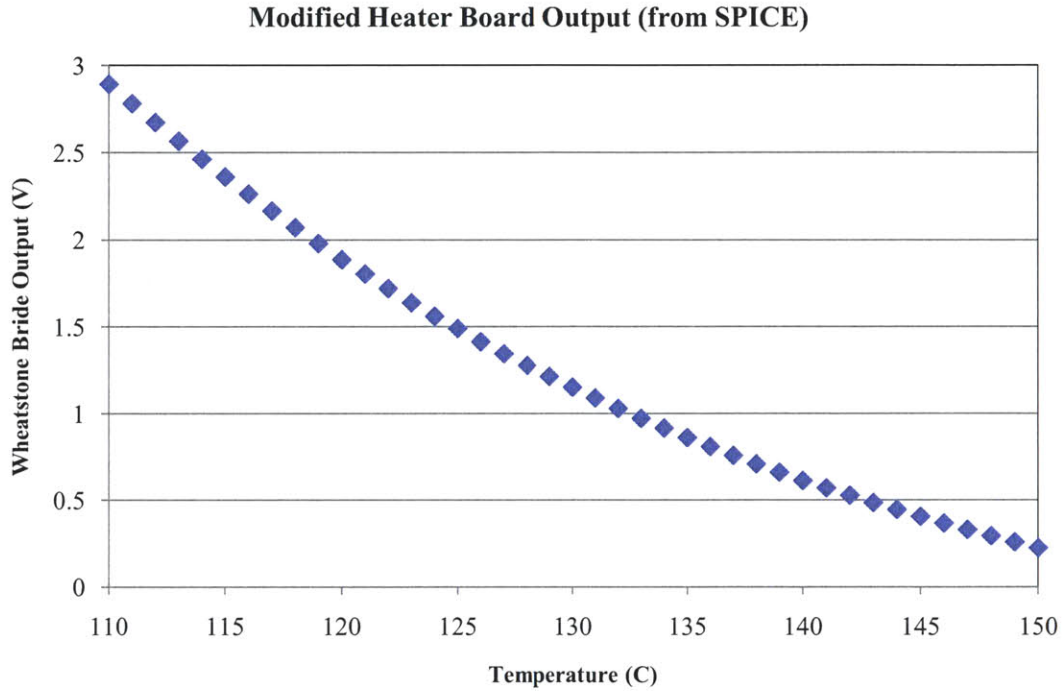
Figure 32: SPICE Simulation Output of Modified Wheatstone Bridge at Temperatures 110-150C

The SPICE simulation models the output from the modified Wheatstone bridge for single degree increments of temperature in the desired 110-150 degree range. Figure 32 shows that a large percentage of the 0-3V input is used in the desired operating regime. This is ideal to allow maximum temperature measurement resolution with the 10-bit A/D converter present on the control board. The resistors were then swapped out on the control board and the modified controller was tested with an additional Omega type K thermocouple installed on the sensor head to verify that the new temperature settings were correct. Long term temperature stability was also tested with the high-voltage electro-optic modulator signal present to assure that there was no crosstalk between the two components of the sensor head. The testing revealed a root mean square error of 0.027 degrees Celsius over a period of two hours (see Figure 33; discrete errors are due to digitization). This comfortably met initial design specifications from Princeton only called for 0.1 degrees Celsius error.

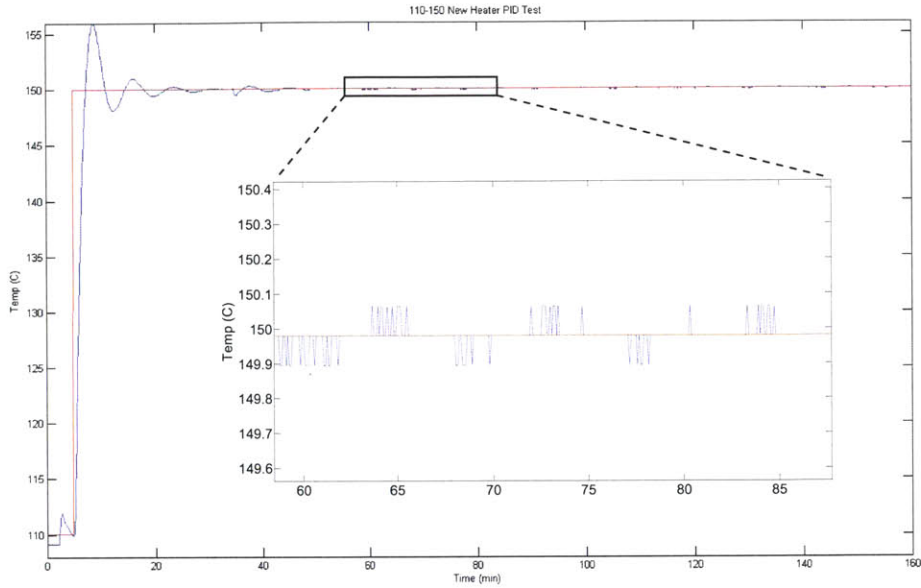Figure 33: Modified Heater Board Performance and Stability[1]

5.5 Optical Train

The optical train is responsible for supplying both the pump and probe beams to all 64 sensors in the sensing array. The optical train setup at Draper (see Figure 34 and Figure 35) delivers roughly 10-20mW to the pump and probe fibers, which is sufficient power to operate two sensors simultaneously. This setup was used for all preliminary testing in this thesis. This train includes the respective lasers, as well as multiple conditioning optics to polarize, align, and control the intensity of the beams. The optics conditioning is exactly the same for the pump and probe beam. The dual-alkali vapor cell design requires a pump laser (Photodigm PH895DBR100T8) at 895nm to address the Cesium D1 line and a probe laser (Photodigm PH795DBR070T8) at 795nm to address the Rubidium D1 line. The optical train for a single wavelength can be seen in Figure 34.

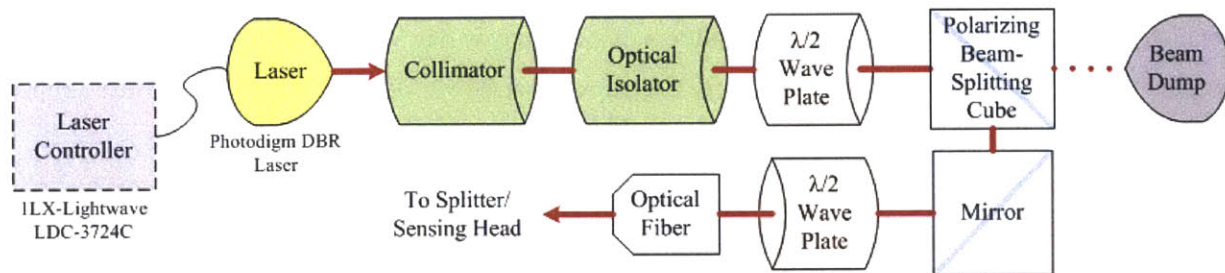Figure 34: Optical Train Schematic

The laser controller (1LX Lightwave LDC-3724C) is responsible for supplying both the current to the laser diode and control over the thermoelectric cooler (TEC) in the laser package. As current is supplied

---

[1] Slight transient at 35-50 minutes due to accidental physical movement of the sensing head; finite deviations in temperature due to digitization

53

to the laser diode, it begins to produce light. The collimator collects the diverging laser light and collimates it into a beam of a constant diameter. The optical isolator then acts as the optical equivalent of an electronic diode and only allows light transmission in one direction. This serves to prevent unwanted optical feedback to the laser. The first half-wave ($\lambda/2$) plate permits fine control of the beam power by splitting the beam between the two exit ports of the polarizing beam-splitting cube. The second half-wave ($\lambda/2$) plate facilitates polarization matching of the laser light with the polarization-maintaining fiber. The mirror simply reflects the conditioned beam into the fiber and serves as an additional degree of freedom to align the polarization axis and x-y location of the beam into the fiber [13].
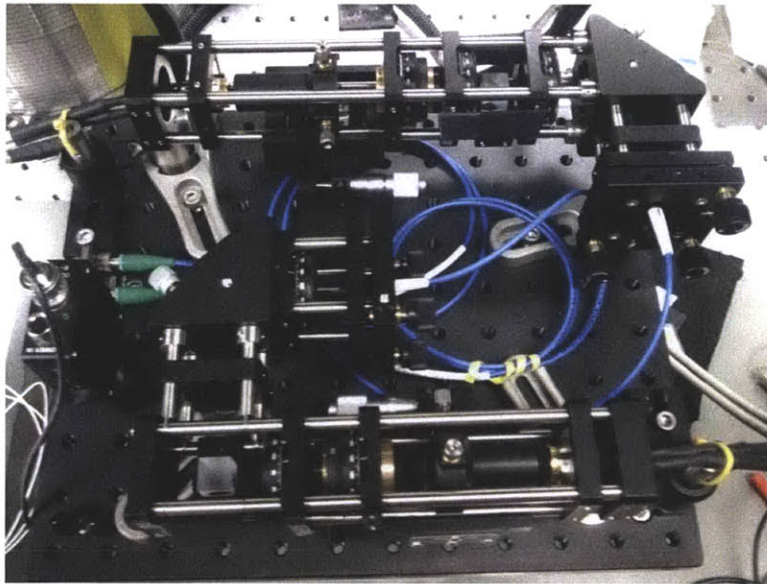
Figure 35: Optical Bench Setup of Pump and Probe Lasers at Draper

The output fiber from the optical train is fed directly into a sensing head if a single sensor is being used. For the full sensing array, a series of beam splitters (two tiers of 8-way splitters = 64 outputs) are used to provide lasers to all 64 sensors. The full array also requires an additional laser amplifier for both wavelength lasers due to signal loss in the splitters (approximately one Watt of laser power pre-splitter is required). This assures that all sensors receive a pump laser power of at least 5mW to assure proper functionality.

The probe output from the sensing head is sent to a photodiode board manufactured by Agiltron. The photodiode board converts the light intensity from the sensing head to a voltage that is fed to the data acquisition system. There is no interfacing with the PC or manual user-input necessary. Each photodiode board has 16 optical fiber inputs. A total of four boards are required for the 64 sensor array. If additional sensors are desired in the future more photodiode boards can simply be added to the system. The preliminary design of the photodiode board and EOM driver can be seen in Figure 36.

Figure 36: Photodiode (left) and EOM Driver (right) Circuit Boards
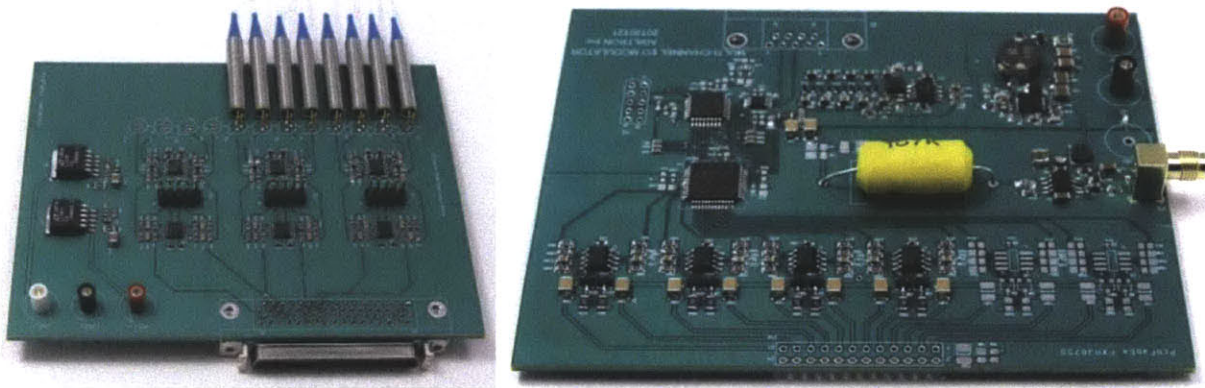
5.6 Magnetic Shielding

As mentioned previously, one of the limits of SERF magnetometers is the requirement of very low residual magnetic fields for proper operation. Therefore, a SERF magnetometer must have the earth's magnetic field nulled in some way for full functionality. There are two methods to achieve this: generally large, well designed passive magnetic shielding or an active method using current to generate a nulling field through the use of Helmholtz coils. The testing at both Draper Laboratory and Princeton University was performed using a combination of both these techniques.

5.6.1 Physical Shields

The testing at Draper Laboratory was performed using a compact 4-layer magnetic shield designed by Twinleaf LLC (Princeton, NJ) and manufactured by the MuShield Company (Londonderry, NH) (see Figure 37). The shield is relatively small at approximately 17 centimeters in outer diameter and 20 centimeters in length, yet has a magnetic shielding factor of 10^6. There is enough room inside to allow testing of two SERF sensors simultaneously. There is also a degaussing coil built into the shield to aid in the removal of residual magnetic fields in the shield before testing.

The shield designed to house the full 64 sensor array is located at Princeton University and is much larger than the shield located at Draper. It is approximately 1 meter in diameter and consists of three layers of μ-metal to aid in magnetic shielding. This large shield has a transverse shielding factor of 10^4. Princeton has also developed a specialized shield with an inner ferrite layer to rest inside of the large shield. The combination of both magnetic shields results in a total shielding factor of about 10^8. This is more than adequate for testing of the full sensing array. The shield also allows a human to fit inside for initial testing of the SERF magnetometer array in a magnetoencephalography application.
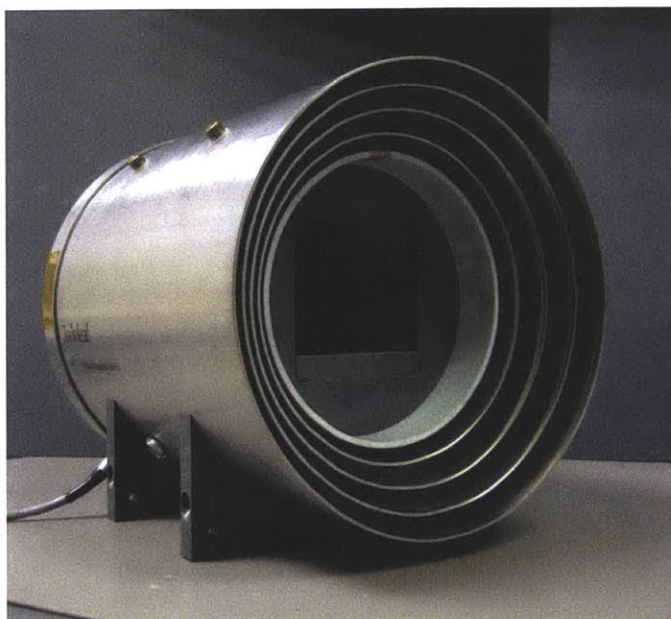
Figure 37: Small four layer magnetic shield used for testing at Draper

5.6.2 Magnetic Coils

Both Draper and Princeton use electromagnetic coils located inside of the magnetic shielding to aid in nulling the earth's field as well as apply modulation to the sensors. The magnetic coils in Draper's testing configuration consist of a flexible printed circuit board that is located inside of the magnetic shield. These coils are connected to the D-tacq analog out card and have control of the X, Y, and Z magnetic field magnitudes. This configuration is adequate for nulling the magnetic field around a single sensor or two sensors in close proximity. However, to null the fields around a large array of sensors spread over a larger area greater magnetic field control is required. For this reason, the large shield at Princeton University has a total of eighteen coils located inside of the shield. This allows full control over the magnetic field in the primary axes as well as full control of the magnetic gradients. Both sets of coils are connected to the analog output card via a National Instruments SCSI-3 cable breakout board and controlled by user-specified inputs from the GUI.

There is a linear relationship between a coil's current and the applied magnetic field. A resistor is put in-line between the analog output card and the coil to control the coil's current range. For the testing performed at Draper Laboratory, the resistors for the X and Z coils are both 11.4kΩ and the resistor for the Y coil is 32.4kΩ (measured). The higher impedance in the Y coil allows for a greater modulation resolution at low voltages. This is beneficial as the sensor is most sensitive in the y-direction and Y modulation will be applied for all sensitivity measurements. The X and Z coils are primarily used for debugging purposes and to nullify the earth's magnetic field.

Chapter 6 – Sensor and System Performance

6.1 Testing Methods

The purpose of the system testing performed at Draper Laboratory is to verify basic system functionality and test all custom electronics and hardware will properly scale into the full 64 SERF magnetometer array assembled at Princeton University. Verification of system performance at Draper consists of assuring that there is no excessive noise that will hinder desired sensor performance when all components are operated simultaneously. The ultimate sensitivity of one SERF sensor head supported by the custom control and data acquisition system is also measured. Princeton University requires an ultimate sensitivity of 1 pT/√Hz at 1Hz for each sensor head in the sensing array to meet the ultimate goals of the DARPA Heterostructural Uncooled Magnetic Sensor (HUMS) program that is sponsoring the sensor development.

Ultimate sensor performance in the full sensing system is measured with all components of the 64 sensor array system in place. The electronics used for testing at Draper consist of the final designs of all circuits described in Chapter 5. However, due to limitations in the number of available sensors only one sensor is controlled for system verification; therefore only one multi-channel board was required to control the sensor (as opposed to the multiple boards necessary to support the full 64-sensor array). The equipment used for testing consists of two heater control boards (one for each sensing head), a heater switchboard, a 12-channel photodiode board (the final design was scaled to 16 channels), and a 16-channel electro-optic modulator board. All electronic components are powered by a standard DC power supply (B.K. Precision model 1761). The optics train described in Section 5.5 and the magnetic shielding and coils described in Section 5.6 are also used. All control was performed through the custom GUI powered by the Draper Simulation Framework (see Chapter 4).

Preliminary testing is performed with a single sensor packaged in a foam insulation enclosure and placed into the magnetic shielding (Twinleaf part number MS-1). The magnetic shield is then fully closed and degaussed through use of the degaussing coil built into the shield and a variable autotransformer (also known as a "variac"). The voltage from the variac is rapidly increased to its maximum and then decreased to zero in a logarithmic fashion to remove residual magnetic fields from the shield. The sensing head is then brought up to a temperature of 110 degrees Celsius and the EOM powered on and modulated using the reference frequency from the acquisition system. Residual magnetic fields from the earth are nulled by the magnetic coils located inside of the magnetic shield based on the sensor output. The magnetic coils are then used to apply a magnetic modulation signal to the sensing head at a specified frequency. The temperature of the sensor is slowly increased until the maximum

output amplitude for a given modulation is achieved. This is the ideal operating temperature and will be different for each sensor (due to minor variances in assembly and optical alignment). The amplitude of the modulation is then reduced until the modulation is no longer discernable from the background noise. This minimum amplitude is directly correlated to the sensor's ultimate performance at the modulation frequency. The modulation amplitude is also used to scale the lock-in output values into units of Tesla.
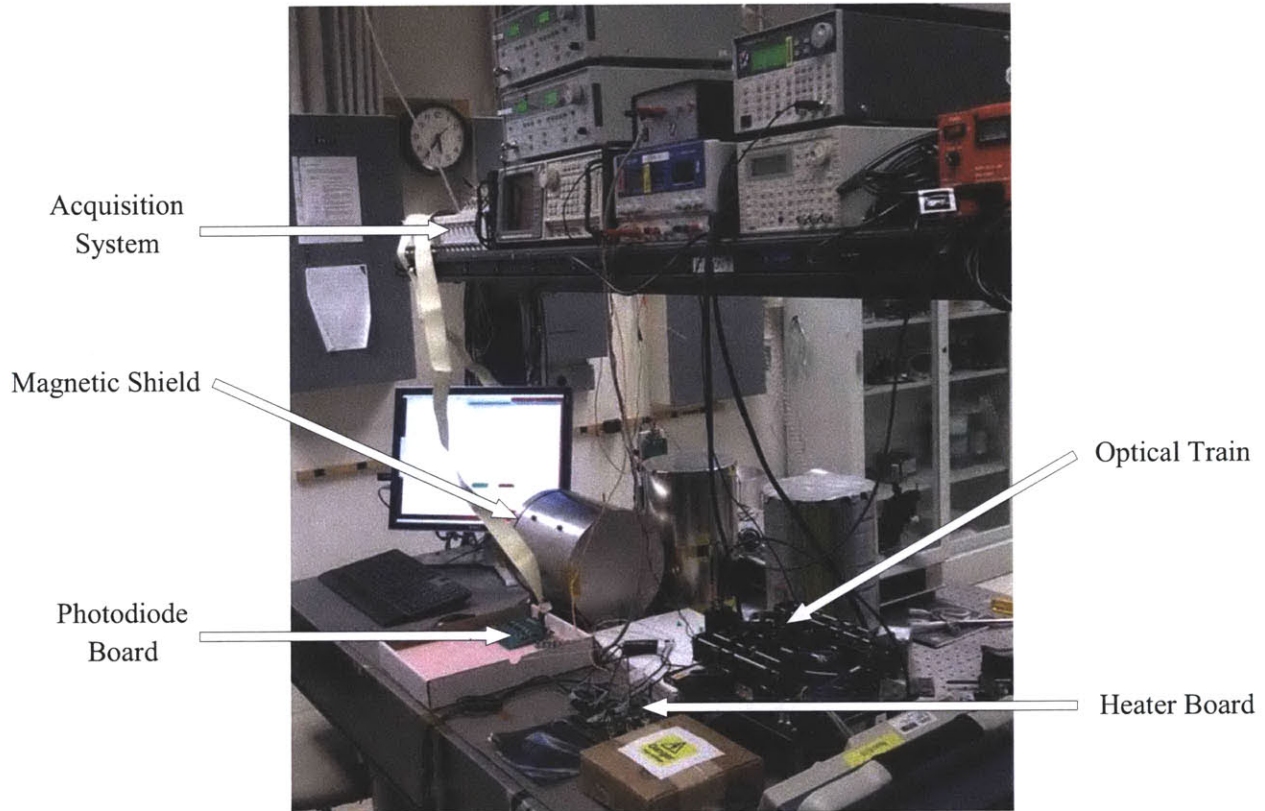

Figure 38: System Set-up to Perform Ultimate Sensitivity Measurements

6.2 Data Analysis

The Draper Simulation Framework software package saves all acquisition system data in a file that was post-processed by Matlab to determine ultimate sensor performance. After applying a significant magnetic modulation to the sensing head (with a signal to noise ratio (SNR) of roughly 100) at a low frequency (~5Hz), the demodulated sinusoid lock-in data is imported into Matlab. The mean of the acquired data is then calculated and used to remove the DC offset from the signal. The amplitude of this signal can be changed to magnetic units through use of a scaling factor determined from magnetic modulation. In our testing setup the coils apply a magnetic field of 0.56 Gauss per Amp (verified with a fluxgate magnetometer). Therefore, if a 2.0 Volt peak-to-peak modulation were applied to the Y-

direction magnetic coil across a 32.4kΩ resistor (see Section 5.6.2) it would correlate to a magnetic field of

$$\frac{0.56 \text{Gauss} / \text{Amp} \times 2.0 \text{Volts}}{32,400 \Omega} = 3.275 \times 10^{-5} \text{Gauss} = 3.275 \times 10^{6} \text{fT}$$

.

That is, a 2.0V magnitude signal produces a maximum magnetic field of 3.275×10^{6} fT. Given the linear relationship between applied voltage and the resulting magnetic field, this relationship provides all voltage-to-magnetic field scaling information.
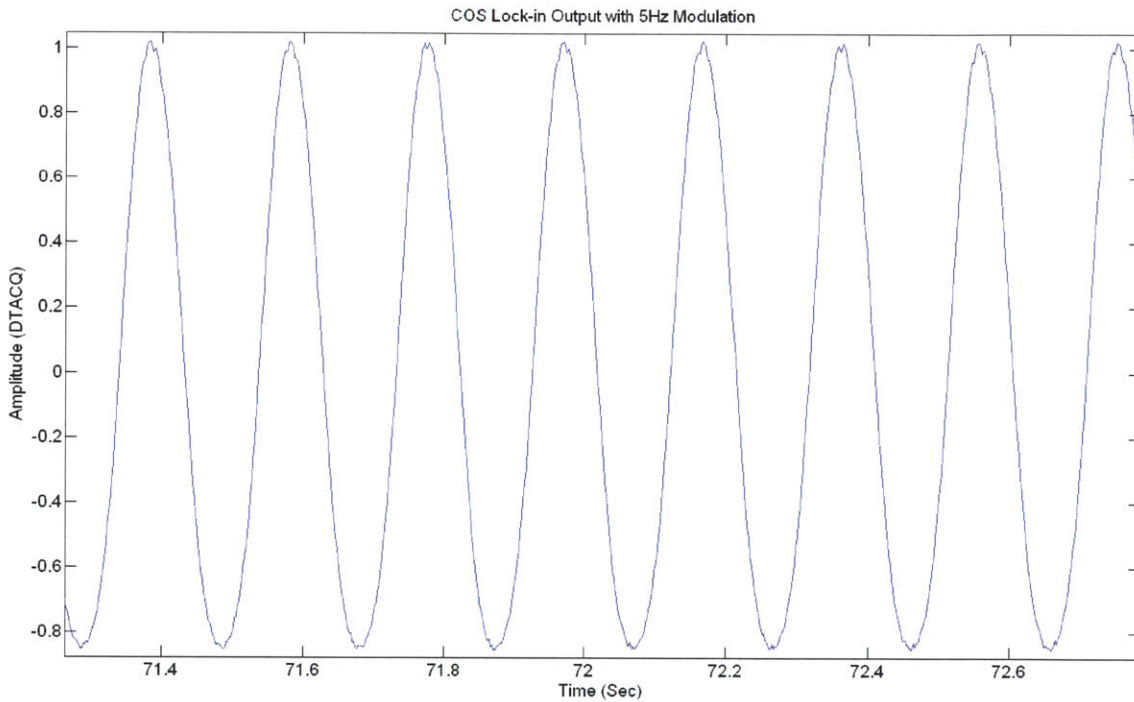

Figure 39: Lock-in Output with 5Hz Magnetic Modulation used to Determine Magnetic Scaling Factor

Figure 39 provides an example of a signal that would be used to determine this scaling factor. This sine wave is the result of a 5Hz magnetic modulation with a 2 volt amplitude. This results in a magnetic scaling factor of

$$\frac{3.725 \times 10^{6} \text{fT}}{1.85 \text{ Amplitude}_{PP}} = \text{Scaling factor of } 1.770 \times 10^{6} \frac{\text{fT}}{\text{ACQ Output in Volts}}.$$

This scaling factor can then be used to perform the FFT of the acquired signal in units of Tesla. The data is then converted to the frequency domain for analysis. The FFT is scaled so the amplitude is independent of the number of points used for processing by averaging the resulting FFT output over a 0.1 Hz frequency bin width, resulting in an output of the square root of the power spectrum (analysis adapted

59

from [14]). The output allows for easy visualization of noise sources and standardizes the data for easy comparison, as the results are unaffected by the length of the Fourier transform. A resulting plot from this analysis (using a 5Hz modulation of 17.5pT peak-to-peak) can be seen in Figure 40.
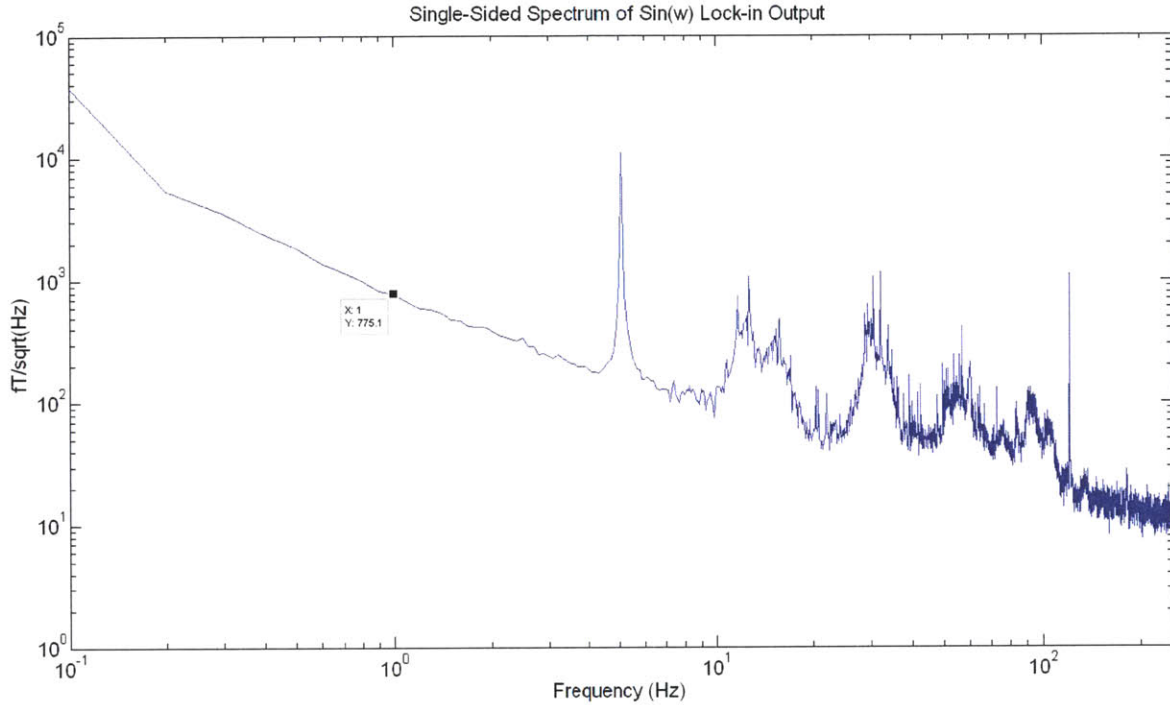

Figure 40: Normalized 5Hz Magnetic Modulation Signal from Sin(w) Lock-in

This measurement of the first sensing head was taken with no filtering or noise compensation and already meets Princeton's criteria of $1pT/\sqrt{Hz}$ sensitivity at 1Hz. The noise baseline at 1 Hz is roughly $775fT/\sqrt{Hz}$. However, sources of noise still will be determined and ultimate sensitivity improved if possible. In the following sections we consider limiting factors in the measured sensor performance.

6.3 Performance Characterization

Due to the large number of electronics and optical components present in the system there are many potential noise sources that can hinder sensor performance. These sources include the EOM driver board/amplifier, the photodiode board, the pump laser, the probe laser, the magnetic coils, and the lock-in amplifier. Each of these custom components was analyzed to determine the electrical or magnetic noise they introduce into the system. Magnetic noise introduced by the heaters is difficult to quantify as the temperature of the cells will decrease rapidly with the heaters powered off. This temperature drift alters

the performance of the EOM and ultimately affects the sensor head's output characteristics. For this reason, heater noise was not quantified.

6.3.1 Noise Characteristics

We begin by analyzing noise from the magnetic coils. Almost all noise from the magnetic coils is due to the voltage signal from the analog output card that supplies the coils. All sensor performance measurements in this thesis were performed with a 0.01V modulation on the Y coil. Therefore, the same voltage signal was connected in parallel to an oscilloscope (Tektronix model TDS3014) and captured for noise analysis. The oscilloscope has a long-term voltage drift specification of ±.02mV which corresponds to a low frequency noise floor of

$$\pm \frac{0.56 \text{Gauss} / \text{Amp} \times .02\text{mV}}{32,400\Omega} = \pm 3.46 \times 10^{-10} \text{Gauss} = \pm 34.6\text{fT}$$

when converted to magnetic field units. This must be kept in mind when analyzing the measured signal.

Regardless of the noise due to measurement, visual observation as well as plotting the FFT revealed that the sinusoidal signal was quite noisy at low amplitudes. A capacitor was added across the Y-coil terminals to act as a basic RC filter. A capacitor of 22nF was chosen, which results in a low pass filter with a corner frequency of ~200Hz. This helps alleviate high frequency noise without significantly attenuating the desired coil modulation. The results from the analog filter (scaled to represent the coil's output magnetic field) can be seen in Figure 41.
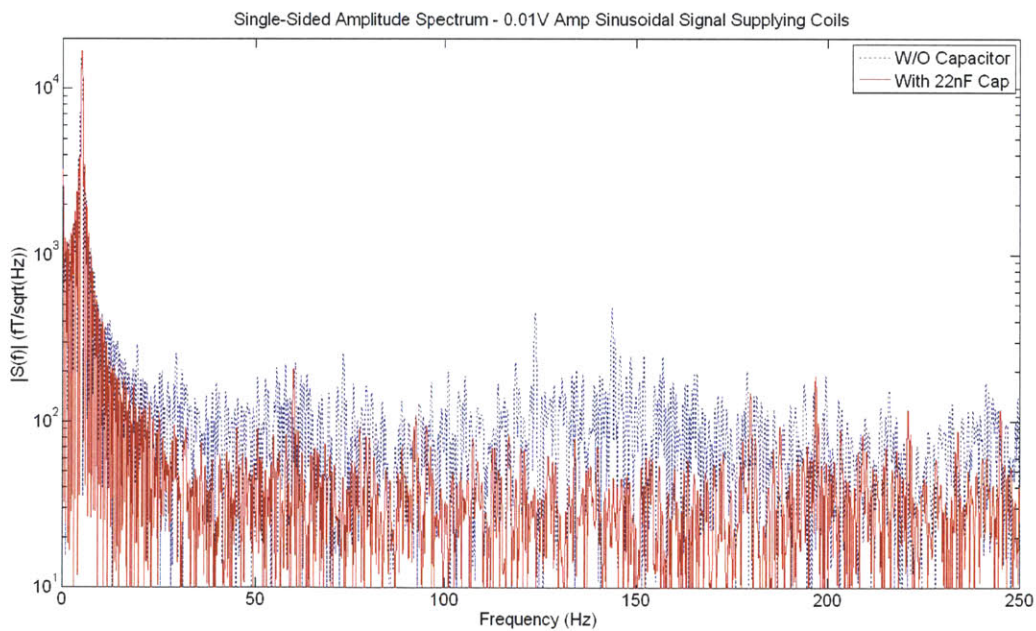

Figure 41: Analog Out Signal Supplying Y-Direction Magnetic Coil

61

This measurement also includes the intrinsic noise from the scope that cannot be removed and shows a total RMS noise of approximately 100fT without the capacitor and 28fT with the capacitor (at frequencies greater than 30Hz). However, with noise from the scope present one can still see a lower magnetic noise level with a capacitor that should directly correspond to better sensor performance. One should also keep in mind that the coils themselves have a frequency response. The only way to measure this is with a very high sensitivity magnetic sensor (such as the SERF sensing head). Since the SERF sensing head has yet to be fully and independently characterized, the frequency response of the coils at low modulation amplitudes is not presented here.

Next, the noise levels from custom electronics in the sensing system are compared to industry standards by verifying the performance of a single sensing head[2]. First, the custom twelve-channel photodiode board supplied by Agiltron Inc is replaced by a single-channel industry standard photodetector (ThorLabs PDA36A photodiode amplifier) to compare the measurement noise between the two. All other equipment and settings were left identical between measurements and the runs performed within five minutes of each other. A comparison of the system performance with a 17.5pT modulation at 5 Hz can be seen in Figure 42.

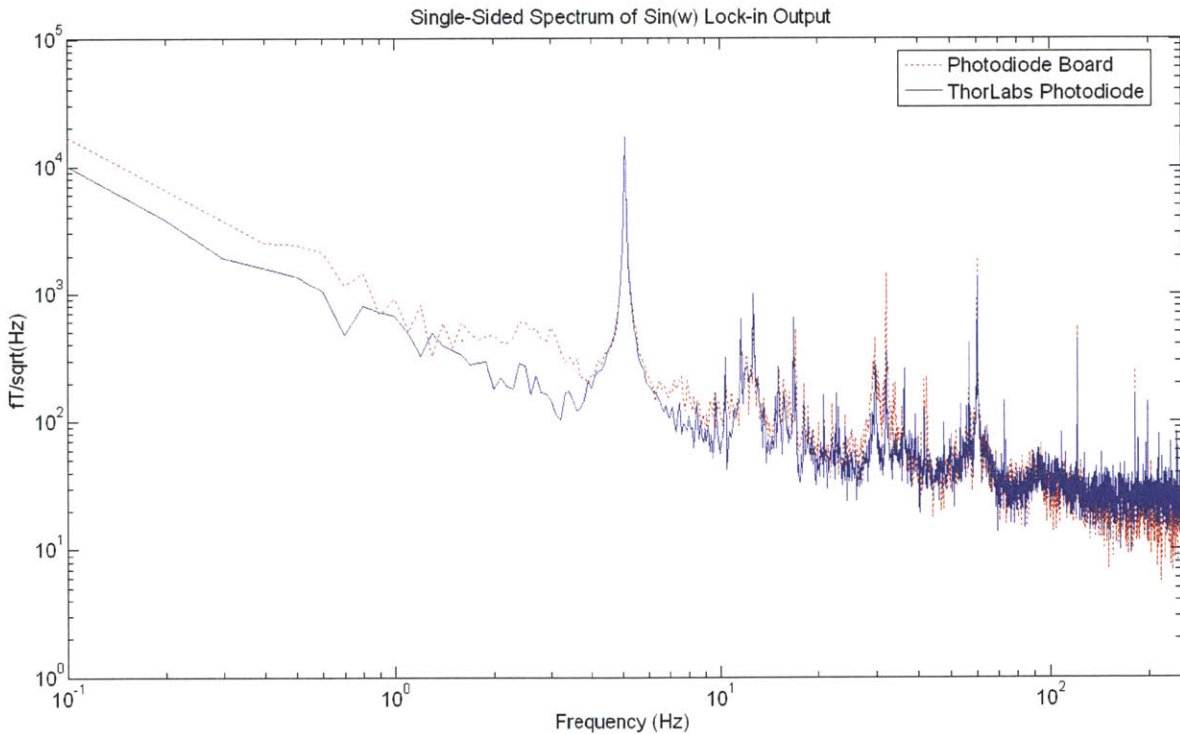Figure 42: Comparison of Sensor Performance with ThorLabs Photodiode

---

[2] All measurements were performed with a cell temperature of 142°C, an EOM DC offset of -68.7V, a 25 kHz modulation signal, and a Y-direction magnetic coil input of 0.01V at 5Hz.

The resulting plot shows that there is little difference between the two measurements. The custom photodiode board has slightly higher noise levels at 30 Hz and at frequencies below ~3 Hz (which is typically described as $1/f$ noise). This $1/f$ noise can be the result of slight environmental changes, such a slow temperature fluctuation of the atomic vapor cell. Noise at all other frequencies up to 100 Hz is roughly the same, and the photodiode board actually demonstrates lower noise levels at frequencies greater than 100 Hz.

After the comparison of photodiode performance, the custom photodiode board was placed back into the sensing system. The custom 16-channel EOM board was then removed from the system and replaced by a standard single-channel amplifier (Matsusada model number HEOPT-0.6B100) that can supply both high-voltage DC offset and provide amplification of the modulation signal from the acquisition system. As before, all other components are left in the same configuration as the full system performance measurement. Figure 43 shows the difference in measurement performance of a 5Hz 17.5pT magnetic modulation.
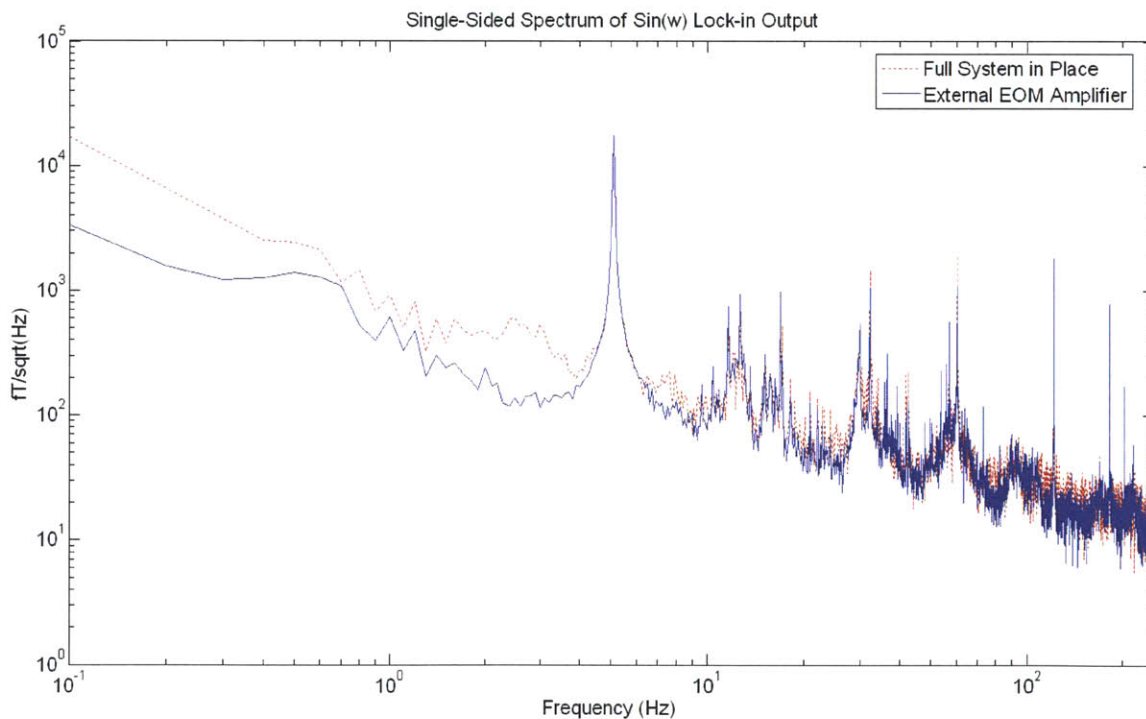
Figure 43: Comparison of Sensor Performance with an External EOM Amplifier

The resulting plot shows slightly better sensor performance at low frequencies with the Matsusada high-voltage amplifier. The custom EOM amplification board provides output as floating voltages while the standard amplifier provides output referenced to ground, which may contribute to the performance discrepancy at low frequencies. As mentioned previously, this noise may also be due to environmental

variables such as temperature fluctuations. While the Matsusada amplifier performs better in the frequency range of interest (~1Hz), it is bulky and expensive compared to the custom Agiltron board. Further, the custom EOM board still meets Princeton's performance requirements of 1pT/√Hz of noise at 1Hz. At frequencies higher than 5 Hz, noise levels between the two amplifiers are approximately the same.

Next, noise from the pump laser within the vacuum cell is quantified. If the pump beam is not perfectly aligned within the sensing head, it can enter the prism at an angle that results in a nonlinear distribution of optical power across the vacuum cell. This can also result in extraneous reflections that couple to the sensing fiber. Excessive pump laser power can also result in complicated alkali-vapor dynamics. To quantify the noise due to the pump laser, two measurements are made back-to-back; one with the pump laser producing standard pumping intensity, and the other with the pump beam completely extinguished. All other conditions are held constant between measurements. The resulting measurements (with a 5 Hz, 17.5pT applied magnetic modulation) can be seen in Figure 44.
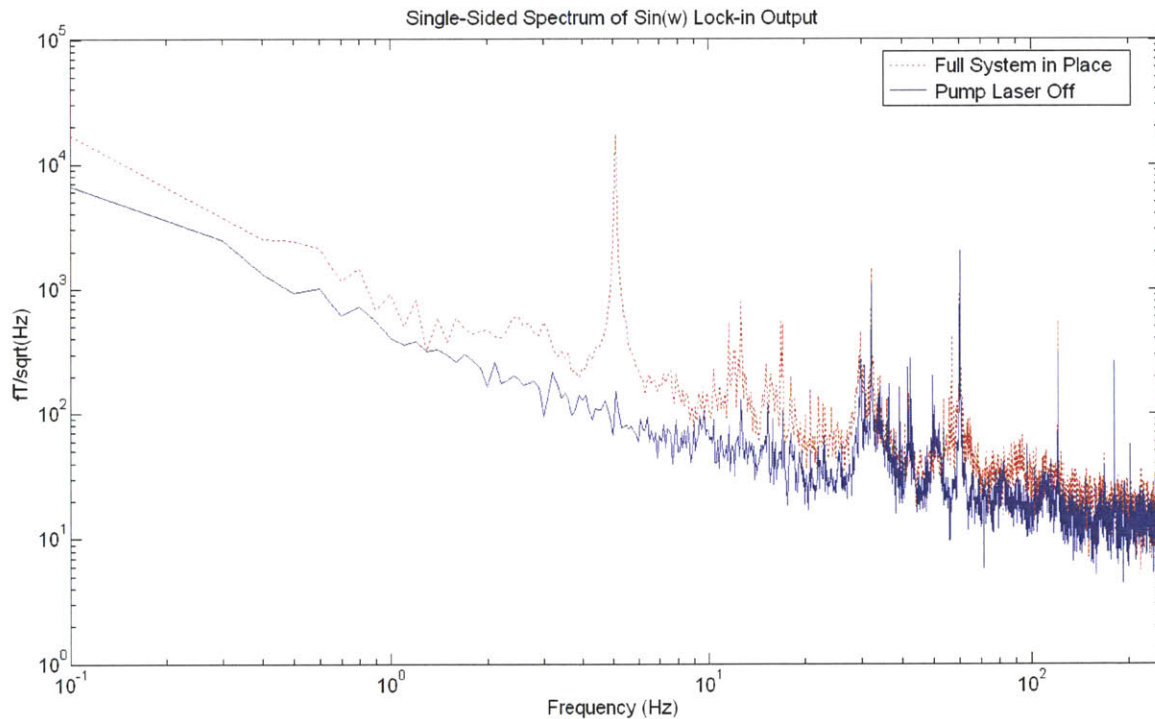
Figure 44: Comparison of Sensor Performance with Pump Laser Powered Off

The resulting plot demonstrates noise from the pump laser may be a valid concern at frequencies less than 30Hz. It is difficult to quantify noise directly associated with the pump laser due to the amplification effect it has on magnetic measurement (this is demonstrated very clearly by the attenuation of signal power at 5 Hz with the pump laser powered off). It cannot be directly discerned whether the low

frequency noise is due to the pump laser directly or environmental magnetic noise. However, analysis of the electrical signal supplying the magnetic coils (Figure 41) does not reveal any excessive noise at these frequencies, so one can reasonably suggest that the pump laser is contributing some low frequency noise.

Finally, the acquisition system is tested to determine the amount of noise added to measurements by the lock-in processing. Unlike the initial validation performed on the acquisition hardware (Section 2.2), this testing is performed with the full sensing system connected and powered. All custom system hardware is used and placed in the same configuration as the full system measurement. Modulation is simply removed from the EOM driver to remove the 25 kHz modulation supplied to the probe laser by the EOM. The resulting output can be seen in Figure 45.
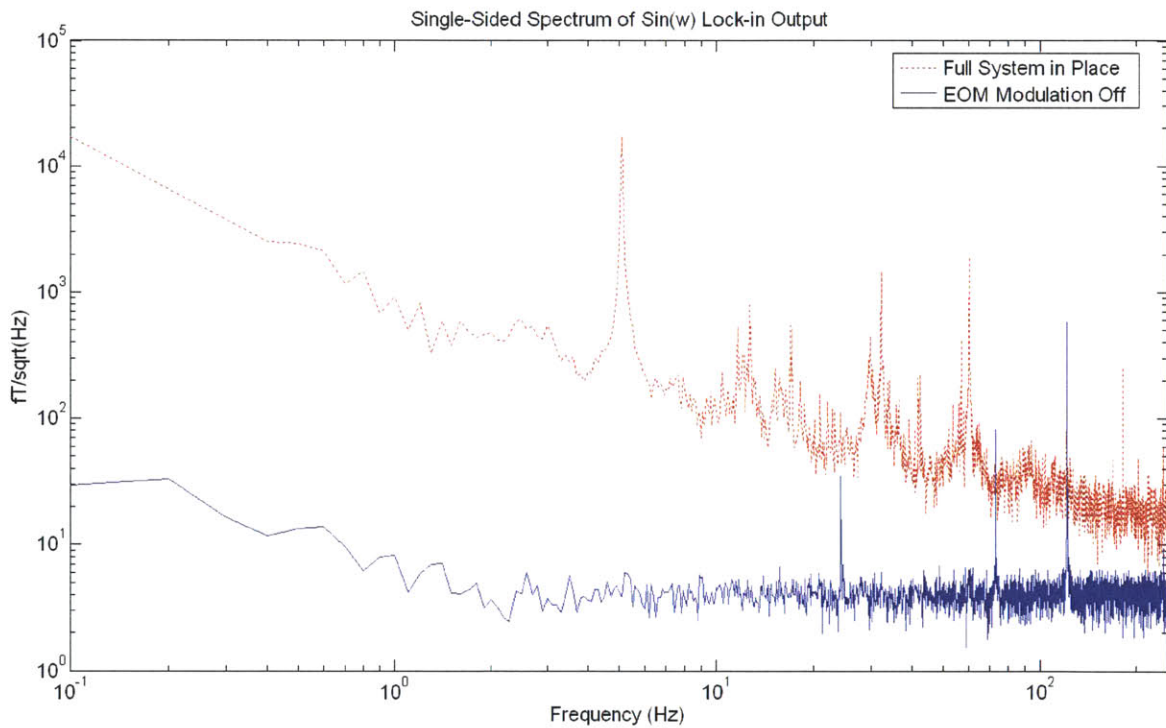

Figure 45: Comparison of Sensor Performance with EOM Modulation Removed

Theoretically the output from the lock-in amplifier should be zero due to the lack of a modulation signal. However, the resulting plot demonstrates that there is still some noise present in the signal. The noise present at higher frequencies at ~5fT is due to the noise floor of the lock-in amplifier (with the current photodiode voltage gain). However, there are three significant noise spikes that most likely correspond to spectral leakage due to the processing of the lock-in. These can simply be removed during post-processing by either a band pass filter or multiple notch filters. It also appears that the lock-in is picking up some DC components of the signal as demonstrated by the slight increase in the noise floor at low

frequencies. This noise is very much below current sensor performance, but should be investigated further as the SERF sensing head performance continues to improve in the future.

6.3.2 Future Improvements

Verification of sensor performance and noise levels using the custom equipment designed to control 64 SERF magnetometers simultaneously has shown that no single piece of equipment is preventing target sensor performance of $1pT/\sqrt{Hz}$ at 1Hz. However, there are a few aspects that should be investigated further as sensor performance improves with continued development. The low frequency noise introduced by the pump laser could be suppressed with improved alignment, beam intensity, and pointing stability. Also, the EOM board should be investigated to verify that there is no voltage drift over time due to the electronics supplying the floating voltage. A test can be performed with the multi-channel board to determine if grounding the voltage results in a change of noise characteristics compared to the floating voltage configuration. Finally, as sensitivity approaches the 20-30 $fT/\sqrt{Hz}$ level with the current acquisition system, the low-frequency noise due to the lock-in picking up changes in DC voltage should be investigated further.

Electronic signal analysis also revealed maximum noise on the order of $200fT/\sqrt{Hz}$ from the magnetic coils. Further analog filtering or a new signal source should be investigated if sensitivity approaches these levels. Also, improved magnetic shielding would require less DC offset from the coils to null residual magnetic fields. This would subsequently allow the use of larger resistors in-line with the coils. Larger resistors will require more voltage to provide magnetic fields, which should also help to reduce magnetic noise levels due to noise in the supplied voltage signal (although noise from the resistors should also be considered).

Although noise due to electronic heating of the cells could not be directly quantified, optical heating could be investigated for future sensing head design iterations. If the temperature of the atomic vapor cell can be stably maintained using optical methods, little to no magnetic noise should be introduced into the system by the heating mechanism. However, this also presents its own set of challenges. Another fiber will need to be fed into the sensing head and stray light from the heating beam could negatively impact system performance.

Chapter 7 – Conclusion

This thesis considers the operation of an array of small, high sensitivity SERF magnetometers that could be used for a variety of applications, including magnetoencephalography and magnetic anomaly detection. In particular, this thesis describes the development and testing of a high-performance control and data acquisition system capable of operating up to 64 sensing heads simultaneously. The control system also has the flexibility to control larger sensing arrays with little modification to existing hardware and software.

Overall, system testing demonstrated magnetometer sensitivity of less than $1pT/\sqrt{Hz}$ at 1Hz with all components of the system in place. The performance of individual multi-channel components of the system was compared to single-channel industry standard equipment. Although both the custom electro-optic modulator control board and the photodiode control board have noise levels slightly above the industry standard, they also provide the flexibility of controlling and measuring up to 64 channels simultaneously while still meeting Princeton University's design specifications.

Future work includes the assembly of a fully functional 64 sensor SERF magnetometer array at Princeton University using the same equipment validated in this thesis. Princeton's superior magnetic shielding and coil control will also demonstrate if the limits of magnetic sensitivity at Draper were due to the simpler magnetic shielding and coils. Operation of the large sensing array will also allow gradiometric measurements (between two adjacent sensors) that should provide sensitivity levels superior to that of a single sensor.

Overall, as research progresses, sensitivity of SERF magnetometers should continue to improve. Manufacturing costs and equipment will also improve and become cheaper, making the sensors ideal for applications ranging from magnetoencephalography and body scanning to magnetic anomaly detection and IED detection. In the future, SERF magnetometers will likely become much more a part of our daily lives.

Works Cited

1. **Haydn, Joseph.** *Dictionary of Dates and Universal Reference, Relating to all Ages and Nations.* London : Edward Moxon, 1841. p. 142.

2. *The Intesnsity of the Earth's Magnetic Force Reduced to Absolute Measurement.* **Gauss, C. F.** 1832, p. 9. Translated by Susan P. Johnson, 1995.

3. *Optical Magnetometry.* **D. Budker, M. Romalis.** 2007, Nature Physics, Vol. 3.

4. *Tunable Atomic Magnetometer for Detection of Radio-Frequency Magnetic Fields.* **I.M Savukov, S.J. Seltzer, M.V. Romalis.** 063004, 2005, Physical Review Letters, Vol. 95.

5. **Ripka, Pavel.** *Magnetic Sensors and Magnetometers .* Boston : Artech House, 2001.

6. *A High-Sensitivity Atomic Magnetometer Unaffected by Spin-Exchange Relaxation.* **J. Allred, R. Lyman, T. Kornak, M. Romalis.** 130801, 2002, Physical Review Letters, Vol. 89.

7. *Detection of NMR Signals with a Radio-Frequency Atomic Magnetometer.* **I. M. Savukov, S. J. Seltzer, M. V. Romalis.** 2007, Journal of Magnetic Resonance, Vol. 185, pp. 227-233.

8. *225 Lock-In Amplifier Guide.* **Bentham Instruments Ltd.** s.l. : Bentham Instruments Ltd, pp. 2-12.

9. *Developments in Alkali-Metal Atomic Magnetometry.* **Seltzer, S.J.** 2008, Dissertation, Princeton University, pp. 1-7, 40-42.

10. **Proakis, John G. and Manolakis, Dimitris G.** *Digital Signal Processing: Principles, Algorithms, and Applications.* 4th. Upper Saddle River, NJ : Pearson Prentice Hall, 2007.

11. *Understand SINAD, ENOB, SNR, THD, THD + N, and SFDR so You Don't Get Lost in the Noise Floor.* **Analog Devices.** s.l. : Analog Devices, 2009, MT-003 Tutorial, pp. 1-6.

12. **Nise, Norman S.** *Control Systems Engineering.* 4th. Hoboken, NJ : John Wiley & Sons, 2004. pp. 531-537.

13. **Hecht, Eugene.** *Optics.* 3rd. Reading, MA : Addison-Wesley, 1998. pp. 330-331, 348-350, 360-366.

14. *A Subfemtotesla Multichannel Atomic Magnetometer.* **I. K. Kominis, T. W. Kornak, J. C. Alfred, M. V. Romalis.** 10 April 2003, Letters to Nature, Vol. 422.